Seismic hazard reappraisal from combined structural geology, geomorphology and cosmic ray exposure dating analyses: The Eastern Precordillera thrust system (NW Argentina)

Lionel Siame, O Bellier, M. Sebrier, D. L. Bourlès, P. Leturmy, Michel Perez, M. Araujo

Geophys. J. Int. (2002) **150,** 241–260

Seismic hazard reappraisal from combined structural geology, geomorphology and cosmic ray exposure dating analyses: the Eastern Precordillera thrust system (NW Argentina)

L. L. Siame,[1] O. Bellier,[2] M. Sébrier,[3] D. L. Bourlès,[2] P. Leturmy,[4] M. Perez[5] and M. Araujo[5]

[1] *UMR Orsayterre* 8616, *bât.* 504-2, *Université Paris-Sud,* 91405 *Orsay cedex, France. E-mail: siame@geol.u-psud.fr*
[2] *CEREGE, Europôle Méditerranéen de l'Arbois,* BP 80, 13545 *Aix-en-Provence Cedex* 04, *France*
[3] *Laboratoire de Tectonique, Université Pierre et Marie Curie, Case* 129, T26-E1, 4 *place Jussieu,* 75252 *Paris Cedex* 05, *France*
[4] *Equipe Structures et Modèles, Département des Sciences de la Terre* 8, *avenue du Parc, Le Campus, Bât. I* 95031 *Cergy-Pontoise, France*
[5] *Instituto Nacional de Prevención Sísmica (INPRES), Roger Ballet,* 5400 *San Juan, Argentina*

Accepted 2002 February 7. Received 2002 January 16; in original form 2001 February 2

SUMMARY

Because earthquakes on large active thrust or reverse faults are not always accompanied with surface rupture, paleoseismological estimation of their associated seismic hazard is a difficult task. To improve the seismic hazard assessments in the Andean foreland of western Argentina (San Juan Province), this paper proposes a novel approach that combines structural geology, geomorphology and exposure age dating. The Eastern Precordillera of San Juan is probably one of the most active zones of thrust tectonics in the world. We concentrated on one major regional active reverse structure, the 145 km long Villicúm–Pedernal thrust, where this methodology allows one to: (1) constrain the Quaternary stress regime by inversion of geologically determined slip vectors on minor or major fault planes; (2) analyse the geometry and the geomorphic characteristics of the Villicúm–Pedernal thrust; and (3) estimate uplift and shortening rates through determination of *in situ*-produced ^{10}Be cosmic ray exposure (CRE) ages of abandoned and uplifted alluvial terraces. From a structural point of view, the Villicúm–Pedernal thrust can be subdivided into three thrust portions constituting major structural segments separated by oblique N40°E-trending fault branches. Along the three segments, inversion of fault slip data shows that the development of the Eastern Precordillera between 31°S and 32°S latitude is dominated by a pure compressive reverse faulting stress regime characterized by a N110° ± 10°E-trending compressional stress axis (σ_1). A geomorphic study realized along the 18 km long Las Tapias fault segment combined with CRE ages shows that the minimum shortening rate calculated over the previous ∼20 kyr is at least of the order of 1 mm yr^{-1}. An earthquake moment tensor sum has also been used to calculate a regional shortening rate caused by seismic deformation. This analysis of the focal solutions available for the last 23 yr shows that the seismic contribution may be three times greater than the shortening rate we determined for the Las Tapias fault (i.e. ∼3 mm yr^{-1}), suggesting that the San Juan region may have experienced a seismic crisis during the 20th century. Moreover, the ramp that controls the development of the Eastern Precordillera appears to be one of the main seismic sources in the San Juan area, particularly the 65 km long Villicúm–Las Tapias segment. A first-order evaluation of the seismic hazard parameters shows that this thrust segment can produce a maximum earthquake characterized by a moment magnitude of ∼7.3 (±0.1) and a recurrence interval of 2.4 (±1.5) kyr. This part of the Villicúm–Pedernal ramp may have ruptured during the $M_s = 7.4$, 1944 San Juan earthquake producing very few surface ruptures and only distributed flexural slip deformation on to the Neogene foreland bedding planes between the Eastern Precordillera and Pie de Palo.

Key words: compressional tectonics, cosmic ray surface exposure, seismic hazard.

1 INTRODUCTION

Obtaining a paleoseismological estimate of the seismic hazard linked to large reverse or thrust faults is a difficult task. Indeed, those faults may generate destructive earthquakes that produce either conspicuous surface ruptures or small and questionable surface displacements, or even no evident surface rupture. That latter case precludes the use of paleoseismological methods, such as trenching of exposed faults and dating displaced strata, to determine earthquake recurrence because large events might be missing. Detecting active reverse faults that may lead to destructive earthquakes thus requires the development of other strategies.

The Andean foreland of western Argentina (Fig. 1) is one of the most seismically active zones of thrust tectonics in the world. In this region, more than 90 per cent of the total continental seismic moment release in the Andean foreland from Ecuador to Patagonia has occurred since 1960 (Chinn & Isacks 1983). The crustal seismicity is characterized by high levels of earthquake activity with hypocentral depths ranging from 5 to 35 km (Smalley & Isacks 1990; Smalley *et al.* 1993) (Fig. 2). Many small to moderate ($M < 6.4$) and several large ($M > 6.4$) earthquakes have struck the region during the last century, most notably the destructive $M_s = 7.4$, 1944, San Juan (Instituto Nacional de Prevención Sísmica INPRES 1977; Kadinsky-Cade 1985) and $M_w = 7.4$, 1977, Caucete (Kadinsky-Cade 1985; Langer & Bollinger 1988) events (Fig. 2). However, direct relationships between major Quaternary faults and historical surface ruptures have not been yet clearly proven.

In order to improve earthquake source characterization and seismic hazard assessments in the area of San Juan, a novel combination of structural geology, geomorphology and exposure age dating approaches have been integrated. We concentrated on one major regional active reverse structure, the Villicúm–Pedernal thrust, where this methodology allows one to: (1) constrain the Quaternary stress regime by inversion of geologically determined slip vectors on minor or major fault planes; (2) analyse the geometry and the geomorphic characteristics of the Villicúm–Pedernal thrust; and (3) estimate uplift and shortening rates through determination of *in situ*-produced ^{10}Be cosmic ray exposure (CRE) ages of abandoned and uplifted alluvial terraces.

2 GEODYNAMICAL AND GEOLOGICAL SETTINGS OF THE SAN JUAN AREA

The Andean foreland of western Argentina (Fig. 1) corresponds to a region of backarc deformation related to the subduction of the Nazca oceanic lithosphere beneath South America. Two depth distributions of earthquake activity characterize the seismicity of this region (Fig. 2). Earthquakes with hypocentral depths at ~100 km demonstrate the flat slab geometry of the Nazca plate beneath South America (Cahill & Isacks 1992; Smalley *et al.* 1993; Engdahl *et al.* 1998; Gutscher *et al.* 2000), whereas earthquakes with hypocentral depth ranging from 5 to 35 km correspond to crustal seismicity between the Precordillera and the Sierras Pampeanas (Smalley & Isacks 1990; Smalley *et al.* 1993), which compose the two main structural domains of this Andean region. The Argentine Precordillera is a thrust-and-fold belt located east of the Frontal Cordillera and the Sierras Pampeanas is an eastern province of thick-skinned basement uplifts (Fig. 1). The N–S trending Argentine Precordillera, which is nearly 400 km long and roughly 80 km-wide, is separated from the Frontal Cordillera by a N–S piggyback basin: the Calingasta-Iglesia Valley (Beer *et al.* 1990; Jordan *et al.* 1993) (Fig. 1). The Andean Bermejo foreland basin separates the Precordillera from the westernmost Pampean basement uplifts consisting of Pre-Cambrian metamorphic rocks (Mirré 1979; McDonough *et al.* 1993; Vujovich & Ramos 1994) (Figs 1 and 2).

The Central Precordillera is a mountainous topography predominantly characterized by a landscape of linear ranges and basins. Reverse thrust faults bound Paleozoic ranges and narrow linear valleys filled with Neogene and Quaternary continental sediments (Baldis & Chebli 1969; Ortíz & Zambrano 1981; Baldis *et al.* 1982; von Gosen 1992; Jordan *et al.* 1993). The Central Precordillera is an East-verging thrust-and-fold belt comprising reverse and thrust faults. In contrast, the Paleozoic and upper Cenozoic strata that compose the Eastern Precordillera are affected by a series of west-verging reverse faults and fault-propagation folds (Zapata & Allmendinger 1996a,b; Zapata 1998). The Miocene foreland basin strata that crop-out in the Eastern Precordillera record the Andean uplift to the west (Johnson *et al.* 1986; Milana 1990; Jordan *et al.* 1993). The Central Precordillera and the Eastern Precordillera form oppositely verging thrust systems on the western and eastern sides of the Matagusanos Valley, respectively (Zapata & Allmendinger 1996a,b; Siame 1998). Whereas thin-skinned, east-vergent structures characterize the Central Precordillera, thick-skinned, west-vergent structures mark the Eastern Precordillera (Fig. 2) (Zapata & Allmendinger 1996a,b). Thrusts in the Central Precordillera developed eastwardly between ~20 and 5 Ma, although some of the easternmost thrusts may be still active (Jordan *et al.* 1993; Zapata & Allmendinger 1996a,b; Siame 1998). During the past 5 Myr, interaction between the Eastern and Central Precordilleras has resulted in a total shortening of ~40 km (Jordan *et al.* 1993; Zapata & Allmendinger 1996a,b).

At ~31°30′S, the crustal seismicity and the numerous Quaternary fault traces observable on both SPOT satellite imagery and aerial photographs indicate that the Eastern Precordillera is the most active side of the Matagusanos Valley (Figs 1 and 2). This major decollement may be connected with ramps that reach the surface on either side of the Matagusanos Valley where two west-verging thrusts can be observed (Fig. 1). Structural analysis based on satellite imagery and aerial photographs show that the Matagusanos Valley narrows dramatically south of the San Juan river, suggesting that the westernmost west-verging thrust of the Matagusanos Valley should connect to the regional Villicúm–Pedernal thrust that bounds the western foothill of the Eastern Precordillera (Fig. 1). Consequently, the Villicúm–Pedernal thrust can be considered to be a major ramp off the decollement located below the Tullúm and Bermejo Valleys (Siame 1998) (Figs 1 and 2).

3 THE EASTERN PRECORDILLERA BETWEEN 31°S AND 32°20′S LATITUDE

3.1 The Villicúm–Pedernal thrust

The Villicúm–Pedernal thrust is a 145 km long, N20°E-trending structure that runs on the western piemont of the Eastern Precordillera between 31°S and 32°20′S latitude, bounding Sierra de Villicúm, Sierra Chica de Zonda and Sierra de Pedernal (Fig. 1). Structural segments separated by oblique N40°E-trending fault branches define the Villicúm–Pedernal thrust (Fig. 1). These segments are the Villicúm, the Las Tapias and the Zonda–Pedernal segments, from north to south, respectively. Both the Villicúm and Las Tapias segments are characterized by a fault trace that clearly

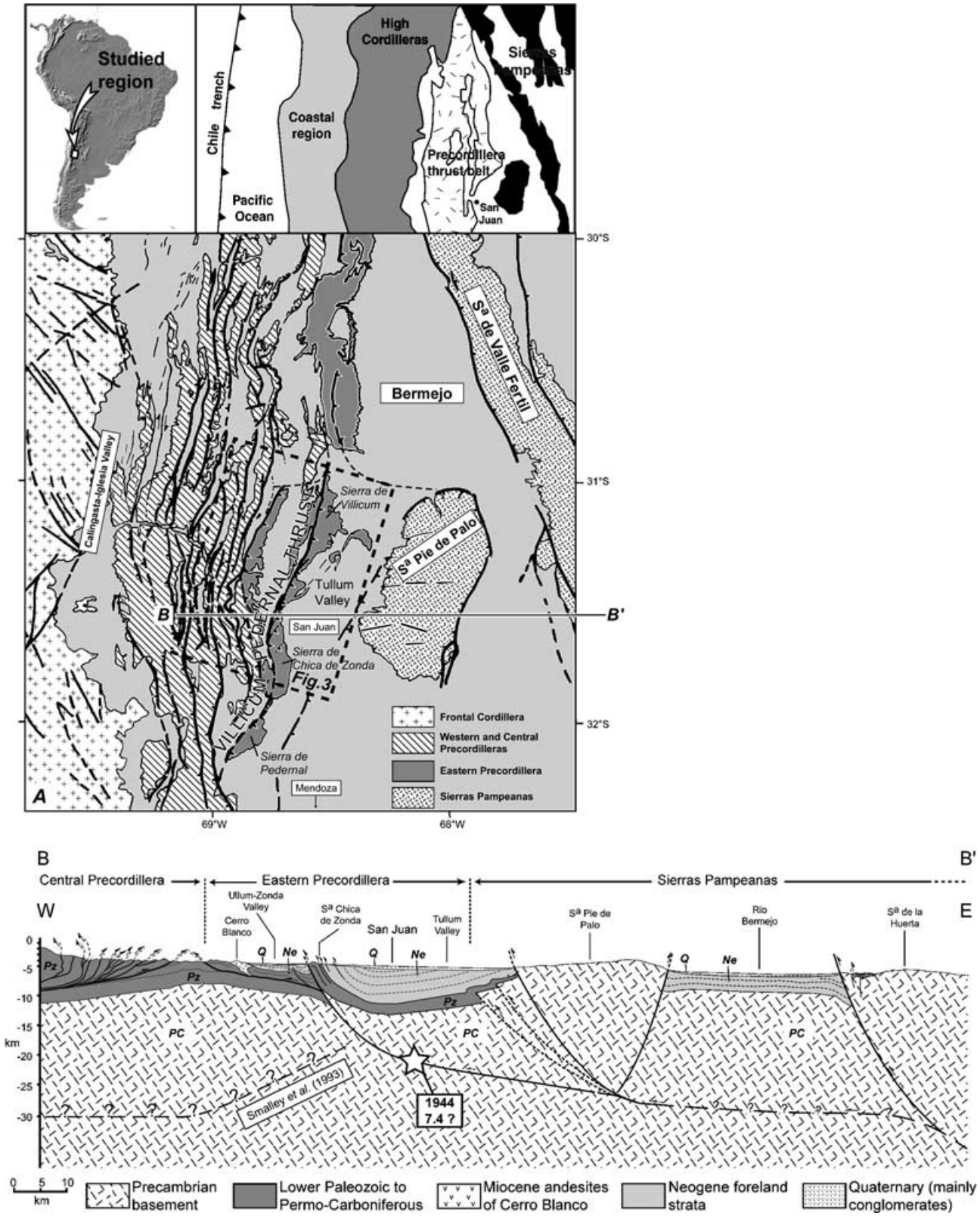

Figure 1. (A) Structural regional map of Argentine Precordillera and western Sierras Pampeanas from Spot and Landsat image analysis. It shows the main structural subprovinces and locates the Villicúm–Pedernal thrust that bounds the western side of the Eastern Precordillera. (B) Schematic regional cross-section at ∼31°30′S latitude showing a thick-skinned deformation front (Zapata & Allmendinger 1996a,b). The left-hand part of the cross-section (Central Precordillera) is from von Gosen (1992). The Eastern Precordillera is bounded by the Villicum-Chica de Zonda thrust structure that ramps into a nearly 25–30 km deep flat decollement towards the east. The decollement depth below Sierra Pie de Palo is constrained from crustal seismicity (Smalley *et al.* 1993). The Tullum Valley, a large syncline structure is mainly deformed by bedding-slip faulting near the eastern piemont of Eastern Precordillera. Sierra Pie Palo is interpreted as an active basement 'pop-up'.

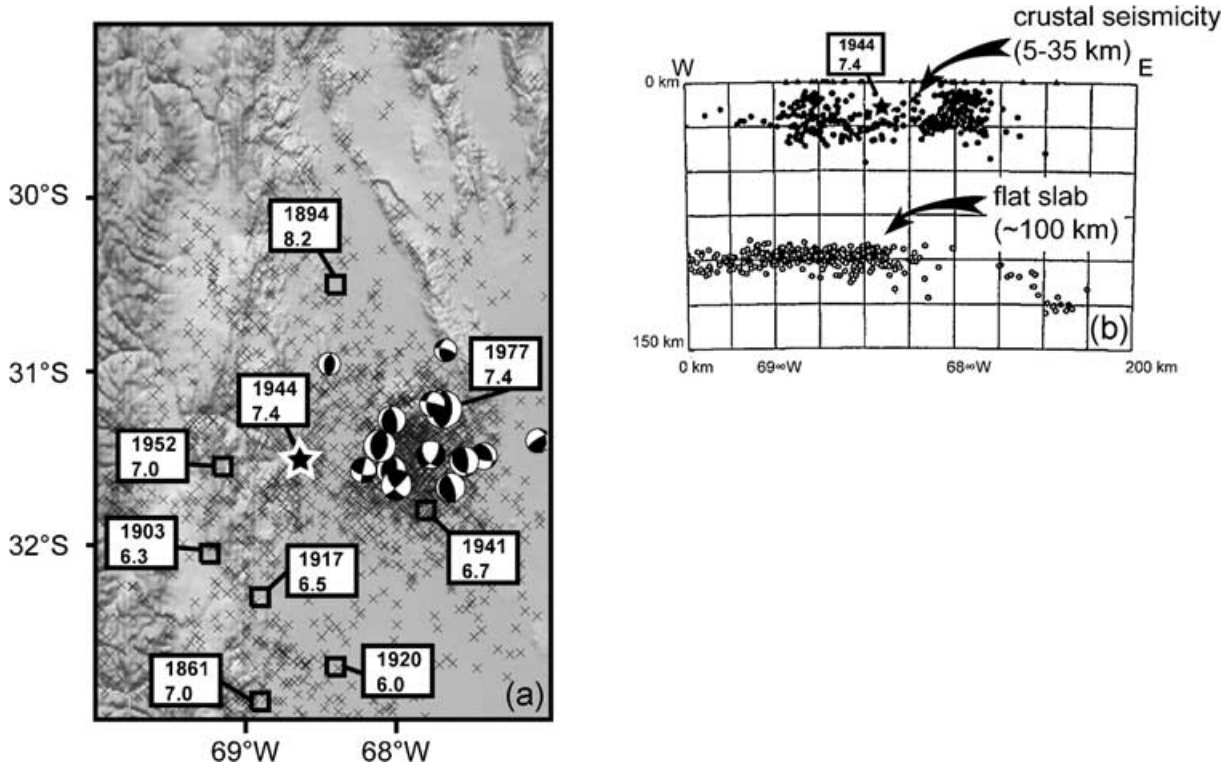

Figure 2. (A) Map of the San Juan region (modified after Smalley & Isacks 1990; Smalley *et al.* 1993) showing the historical seismicity from SISRA catalogue (dated open squares, 1944 location from Kadinsky-Cade 1985), 1973–2000 crustal seismicity from NEIC preliminary determination epicentres (small black crosses), and focal mechanisms (Chinn & Isacks 1983; Kadinsky-Cade 1985); Dziewonski *et al.* 1987. (B) cross-section showing shallow (solid circles) and intermediate-depth (open circles) earthquakes (modified after Smalley *et al.* 1993).

affects the Quaternary deposits, whereas, the fault trace of Zonda–Pedernal segment is less conspicuous.

3.1.1 Villicúm segment

The Villicúm segment is a N22°E-striking linear pattern that parallels Sierra de Villicúm bounding the eastern side of Matagusanos Valley. Along its entire length, the thrust trace affects usually the strata up to the Quaternary deposits. This 47 km long strand starts at the northern termination of Villicúm faulted anticline and extends southwardly to the southern end of Sierra de Villicúm, where two N40°E-trending reverse faults branch, defining a tectonic slice, mark its southern termination.

3.1.2 Las Tapias segment

The second segment, the Las Tapias fault (LTF), is 18 km long and extends with the same N22°E trend between the southern Sierra de Villicúm and the northern Sierra Chica de Zonda fault branches (Fig. 1). In the low-lying region localized between the Sierra de Villicúm and the Sierra Chica de Zonda, the LTF affects Quaternary alluvial deposits that overly unconformably the Neogene foreland strata and forms discontinuous and degraded west-facing scarps (Fig. 3). Minor N40°E-trending topographic features, marked by roughly 1 m high and 1–5 km long scarps, also affect the Quaternary deposits in the LTF area (Fig. 3). These topographic features strike obliquely to the major N22°E-trending LTF and can be regarded as the continuation, within the Quaternary deposits, of the N40°E-trending oblique faults that affect the southern end of Sierra de Villicúm. Both sets of faults at the southern Sierra de Villicúm and the northern Sierra Chica de Zonda are bedding-parallel (Siame 1998), and interpreted as flexural-slip faults.

3.1.3 Zonda–Pedernal segment

The Zonda–Pedernal segment is 80 km long and parallels Sierra Chica de Zonda and Sierra de Pedernal (Fig. 1). This segment starts from the northern Sierra Chica de Zonda fault branch and extends southwardly along the western flank of Sierra Chica de Zonda. The mountain front is not as regular and linear as along the northern segment of Villicúm–Pedernal thrust. Indeed, the western side of Sierra Chica de Zonda is sinuous and discontinuous. In addition, the Quaternary deposits that skirt the western bajada of this mountain range are not conspicuously affected by any fault trace. South of Sierra Chica de Zonda, the thrust seems to disappear and to be relayed by the Sierra de Pedernal anticline, which can most probably be interpreted as a fault-propagation fold. Sierra de Pedernal anticline marks the southern end of the Zonda–Pedernal segment (Fig. 1).

3.2 Stress regime along the Quaternary segments of the Villicum–Pedernal thrust

In order to determine the state of stress along the Quaternary segments of the Villicúm-Perdernal thrust during the westward thrusting of the Eastern Precordillera (Siame 1998), a quantitative inversion of fault-slip data populations measured at individual sites

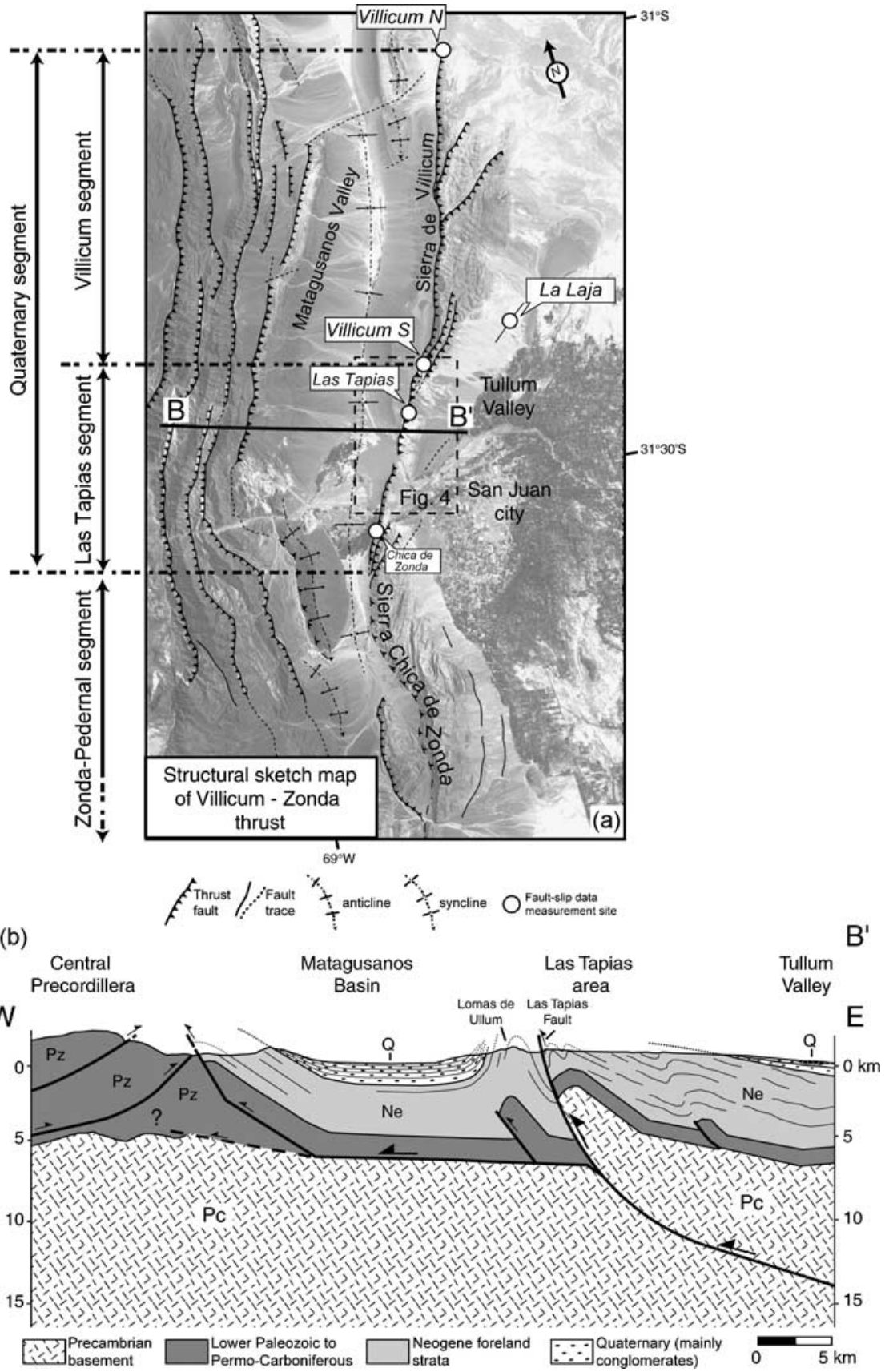

Figure 3. (A) Structural map of the 65 km long Quaternary segment of the Villicúm–Pedernal thrust overlain on Landsat TM showing fault slip data sites of measurements. (B) Schematic cross-section showing the geometry of the Matagusanos Valley. The Lomas de Ullum, and the Las Tapias fault are interpreted as ramp off from the flat thrust located beneath the Matagusanos Basin.

(Fig. 3) has been computed using a method proposed initially by Carey (1979).

3.2.1 Inversion of slip-faulting data for stress regime determination

Constraints on the stress regime during the deformation in the Eastern Precordillera are provided by inversions of fault kinematics on minor or major fault planes. The kinematics of a fault population can be defined using the striations observed on the fault planes. Assuming that the slip vectors represented by the striations occur in the direction of the maximum resolved shear stress on each fault plane (see Bott 1959) and minimizing the angular deviation between a predicted slip vector (τ) and the striation (s) measured in the field, the observation of numerous fault planes can be inverted to compute a mean best-fitting deviatoric stress tensor (see Carey & Brunier 1974; Carey 1979; Angelier 1990; Mercier *et al.* 1991). This method supposes that rigid block displacements are independent. The inversion results include the orientation (azimuth and plunge) of the three principal stress axes of a mean deviatoric stress tensor and a stress ratio $R = \frac{\sigma_2-\sigma_1}{\sigma_3-\sigma_1}$, which is a linear quantity describing the relative stress magnitude. The principal stress axes, σ_1, σ_2 and σ_3, correspond to the compressional, intermediate and extensional deviatoric stress axes, respectively. Taking into account the mechanical assumptions, the computed stress ellipsoid is 'co-axial' with the strain ellipsoid.

Results of stress inversions are generally considered to be reliable if 80 per cent of the angular deviations (s, τ) are less than 20° and if the computed solution is stable. Any inversion thus requires at least four independent fault sets to quantify the orientation of the principal axes and the stress ratio R. Ideal sets of data contain faults dipping in two directions with distinct strike directions, not just a continuum of strikes around a single mean direction (Bellier & Zoback 1995). As proposed by Bellier & Zoback (1995), the stress regime can be computed from poorly distributed fault sets with the additional assumption that one of the stress axes is purely vertical, consequently there are only two unknowns: the orientation of one of the horizontal stresses and the stress ratio.

3.2.2 Results

Sites of fault slip-vector measurements are shown in Fig. 3 and are listed in Table 1. Fault striae have been measured in the Miocene foreland strata of the Bermejo Basin, and in the Cambrian limestones of the Sierra de Villicúm and Sierra Chica de Zonda. Growth strata studies further north have shown that the Eastern Precordillera began to grow 2.6 Ma (Zapata & Allmendinger 1996b). Moreover, as demonstrated by the occurrence of Quaternary faults and shallow seismicity, the Eastern Precordillera is still active (Smalley & Isacks 1990; Smalley *et al.* 1993) (Fig. 2). The current study allows the stress regime associated with the growth of the Eastern Precordillera to be determined, and the present-day state of stress acting along the Villicúm–Pedernal thrust to be inferred. The set of stress tensors determined from fault-slip measurements across the Sierras de Villicúm and Chica de Zonda are remarkably consistent with the stress tensors deduced from inversion of data collected along the Loma de Las Tapias. They correspond to a reverse faulting stress regime (vertical σ_3-axis) characterized by a WNW-trending σ_1-axis.

Sierra de Villicúm and Sierra Chica de Zonda

The Miocene strata that crop-out in the northern termination of the Sierra de Villicúm are composed of a basal conglomerate and alternating red sandstones and shales of the Río Salado Formation (e.g. Milana 1990). The Río Salado Formation was deposited in the Andean foreland basin between 18 and 16.5 Ma (Milana 1990) and overlies unconformably Cambrian limestones of the La Laja Formation (e.g. Bordonaro 1986). These limestones form the inner core of the Villicúm and Chica de Zonda mountain ranges (Figs 2 and 3). The inversion of the fault-slip data sets measured along the Sierra de Villicúm and Sierra Chica de Zonda yield a very consistent state of stress results (Fig. 4). At *Villicúm Norte,* the Miocene strata record a stress regime with a N113°E-trending compressional axis (σ_1). Striae orientations measured in the basal conglomerate agree with those measured in the overlying red sandstones; they indicate a N106°E-trending compressional axis (Fig. 4). The

Table 1. Results of stress tensor inversion from the geologically determined slip data along the Eastern Precordillera and in the Lomas de Las Tapias area. N corresponds to the number of slip-data used for the inversions. Deviatoric principal stress axes $\sigma_1, \sigma_2, \sigma_3$ are the compressional, intermediate and extensional deviatoric stress axes, respectively. They are specified by azimuths (Az) measured clockwise from the north. Plunge (dips) are measured from horizontal. $R = (\sigma_2 - \sigma_1)/(\sigma_3 - \sigma_1)$ is the stress ratio of the deviatoric stress tensor. $n(\tau, s)$ <20° refers to the percentage of deviation angle lower than 20°. The mean deviation angle is M.D. $= \Sigma(\tau, s)/N$, where (τ, s) is the angle between the predicted slip vector, τ, and the observed slip vector, s. The standard deviation of the deviation angle is S.D.$= \{(\Sigma(\tau, s)^2)/N\}^{1/2}$. Qty refers to the quality of the stress inversion: +indicates a well-constrained inversion, i.e. when $N > 11$, M.D. $<$ 13, M.D. $<$ S.D. $<$ 3/2 M.D., 70° $< \alpha_v$ plunge $<$ 90°, α_{hmin} and α_{hmax} plunges $<$ 20° (e.g. defined by Bellier & Zoback 1995); —, indicates an inversion result that did not meet the quality criteria defined above.

Site names	N	σ_1 Azimuths	Dip	σ_2 Azimuths	Dip	σ_3 Azimuths	Dip	R	$n(t,s) < 20°$ per cent	M.D.	S.D.	Qty	Sedimentary formation	Age
Villicum Norte (1)	28	113	5	204	14	3	75	0.3	86	11.7	14.2	+	Rio Salado	Miocene
Villicum Norte (2)	9	286	10	17	7	141	78	0.5	100	3.9	4.7	−	La Laja	Cambrian
Villicum Sur	18	102	0	192	1	10	89	1.0	72	15.6	18.7	−	La Laja	Cambrian
Tapias no 1	47	120	3	30	2	260	86	0.5	70	15.1	17.4	−	La Laja	Cambrian
Tapias no 2	22	110	5	201	5	331	83	0.7	100	6.4	8.1	+	Ullum	Miocene
Tapias no 3	12	104	8	13	4	257	81	0.6	100	5.3	6.6	+	Ullum	Miocene
*La Laja**	7	111	0	201	0	334	90	0.5	100	5.4	7.1	+	Ullum	Miocene
Chica de Zonda	34	99	2	8	8	204	81	0.3	71	14.8	18.4	−	La Laja	Cambrian
Mean σ_1 azimuth		108 ± 4												
Mean σ_1 dip		7.0 ± 3.6												

*Fixed inversion (see text).

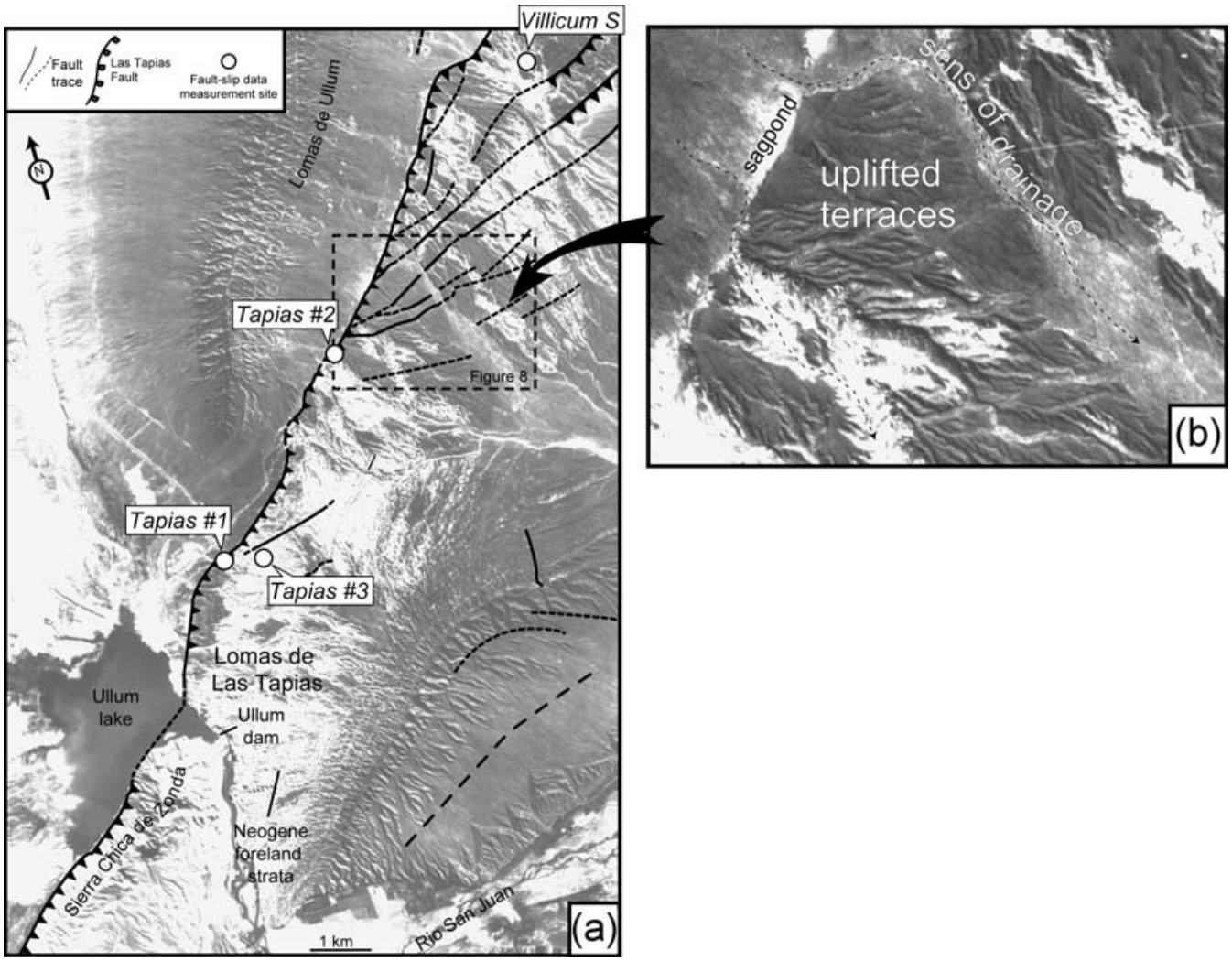

Figure 4. (A) Structural map of the Las Tapias fault shown on an aerial photograph centred on the low-lying region between Sierra de Villicum and Sierra Chica de Zonda. The individual sites of fault-slip data measured along the northern segment are located by open circles. (B) Enlarged view of the alluvial deposits affected by the Las Tapias fault (see Fig. 9 for a detailed map).

orientations of σ_1 computed from the striae measured in the Cambrian limestones along the entire Quaternary segment bounding the Eastern Precordillera (*Villicúm Norte,* N106°E; *Villicúm Sur,* N102°E and *Chica de Zonda,* N99°E) are homogeneous and consistent with the N113°E-trending σ_1 orientation computed from the striae measured in the Miocene strata (Fig. 4). During the growth of the Eastern Precordillera, the orientation of the compressional stress axis (σ_1) has been roughly perpendicular to the N20°-trending Eastern Precordillera.

Lomas de Las Tapias

The low-lying region between the Sierra de Villicúm and the Sierra Chica de Zonda is composed of Neogene red sandstones and shales from the Ullúm formation (e.g. Luna 1988). In the Lomas de Las Tapias, the LTF displaces the Quaternary alluvial deposits that overlie unconformably the Ullúm formation red beds. In this area, fault-slip data have been measured at three individual sites (Fig. 3). *Tapias* no 1 and *Tapias* no 2 are located in the fault zone, whereas *Tapias* no 3 is located in the hanging wall. Site *Tapias* no 1 offers the opportunity to consider the evolution of the stress regime during folding (Figs 5 and 6). At this location, numerous apparently normal fault-slip data are associated spatially with the more abundant reverse faults. These apparent 'normal' fault-slip data are localized in the area where the stratification is vertical (Fig. 6). Taking this dip into account, restoration of the apparent normal fault-slip data yields reverse dip-slip and oblique-slip fault data set, which yield a N123°E-trending σ_1-axis (Fig. 6). These fault-slip data thus belong to an early stage of the deformation and have been rotated during folding. Because they predate folding, these data suggest strongly stability of the stress regime during the fold-and-thrust development with a N120°E-trending compressional axis (Fig. 5). Fault-slip data at site *Tapias* no 2 and no 3 have been measured in the red sandstones from the Ullúm formation that crops out near the fault scarps. At these sites, strata recorded a stress regime with N110°E- and N104°E-trending σ_1-axes, respectively (Fig. 5).

3.2.3 Conclusions concerning the stress regime in the Eastern Precordillera at ∼31°30′S latitude

Inversion of fault-slip data consistently demonstrates that the reverse-faulting stress regime acting during the growth of the

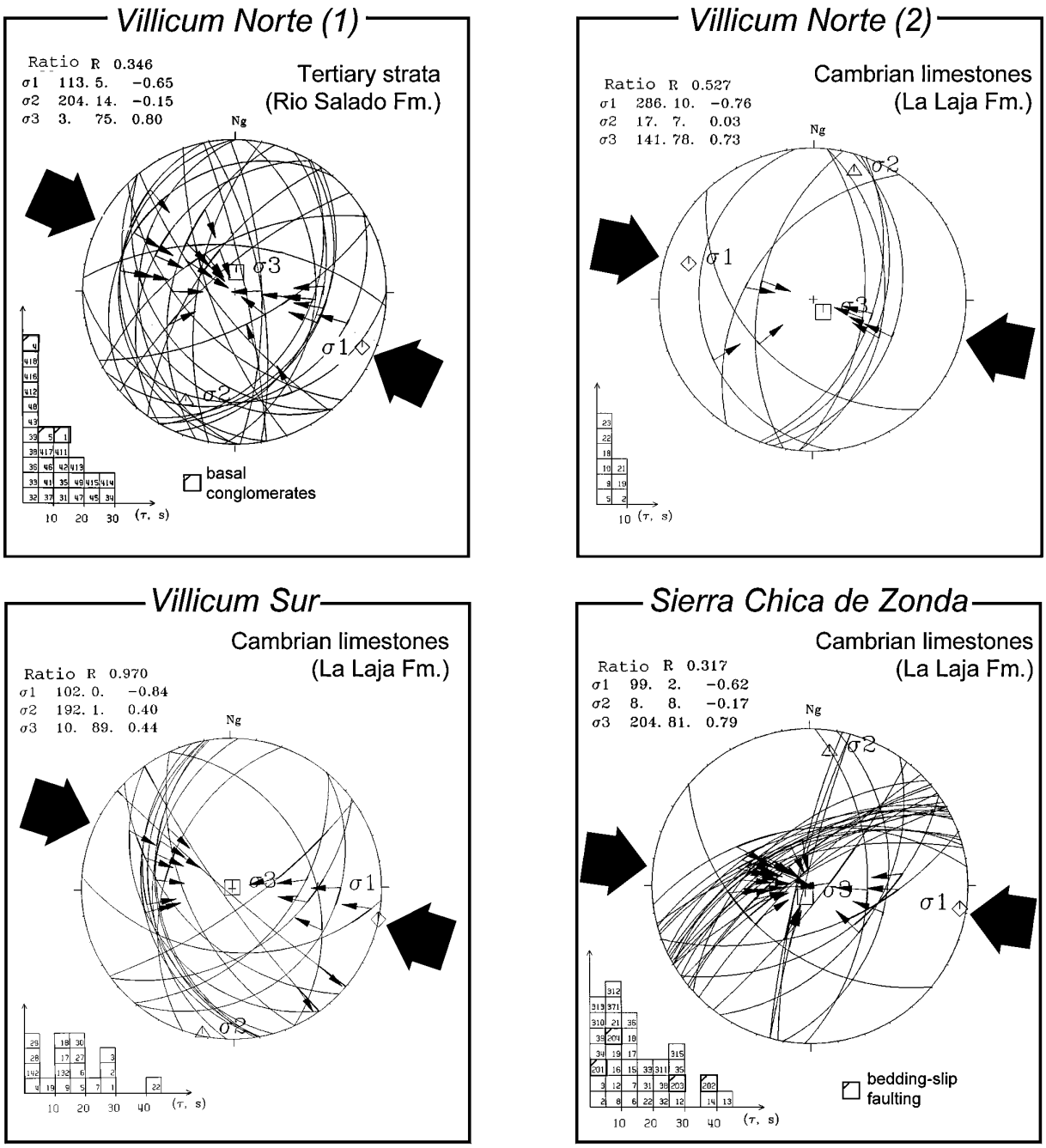

Figure 5. Lower-hemisphere stereoplots of reverse faulting along the Quaternary segment of the Villicúm–Pedernal thrust together with inversion results. Individual fault planes and measured slip vectors at each site are plotted, arrows on fault planes point in directions of horizontal azimuth of the slip vectors. Stress axes obtained by inversions are shown by diamonds (σ_1), triangles (σ_2) and squares (σ_3). Histograms show distribution of deviation angles between the measured 's' and the predicted 'τ' slip vector on each fault plane. Large arrows outside stereoplots give the azimuth of the maximum horizontal stress (σ_1). Inversions of fault-slip sets measured all along the Quaternary segment of the Villicúm–Pedernal thrust yield consistent results, indicating a reverse-faulting stress regime with mean s_1 axis trending N110 ± 10°E.

Eastern Precordillera is remarkably spatially homogeneous and temporally stable. The spatial homogeneity is demonstrated by the stress regimes computed from fault-slip data measured along strike. The temporal stability is demonstrated at the site *Las Tapias* no 1 where pre-folding fault-slip data are in good agreement with the later fault-slip data measured at sites *Las Tapias* nos 1–3. Moreover, the stress regimes in the Las Tapias area are based on fault-slip data measured along the LTF scarps (see below), that is along one of the most recent strands of the Eastern Precordillera. One can thus consider that the stress regime computed for the Las Tapias area is representative of the present-day stress regime. To better constrain this present-day stress regime, we focused on the La Laja fault area (Figs 1 and 8). The La Laja fault is a N55°E-striking linear reverse fault located in the eastern bajada that skirts the piedmont of southern Sierra de Villicúm (Fig. 1). Even though the fault trace is not conspicuous along its entire length, the La Laja fault is most probably parallel to the Neogene bedding that is slightly oblique with respect to the LTF segment (Fig. 1). Like the N40°E-trending oblique reverse

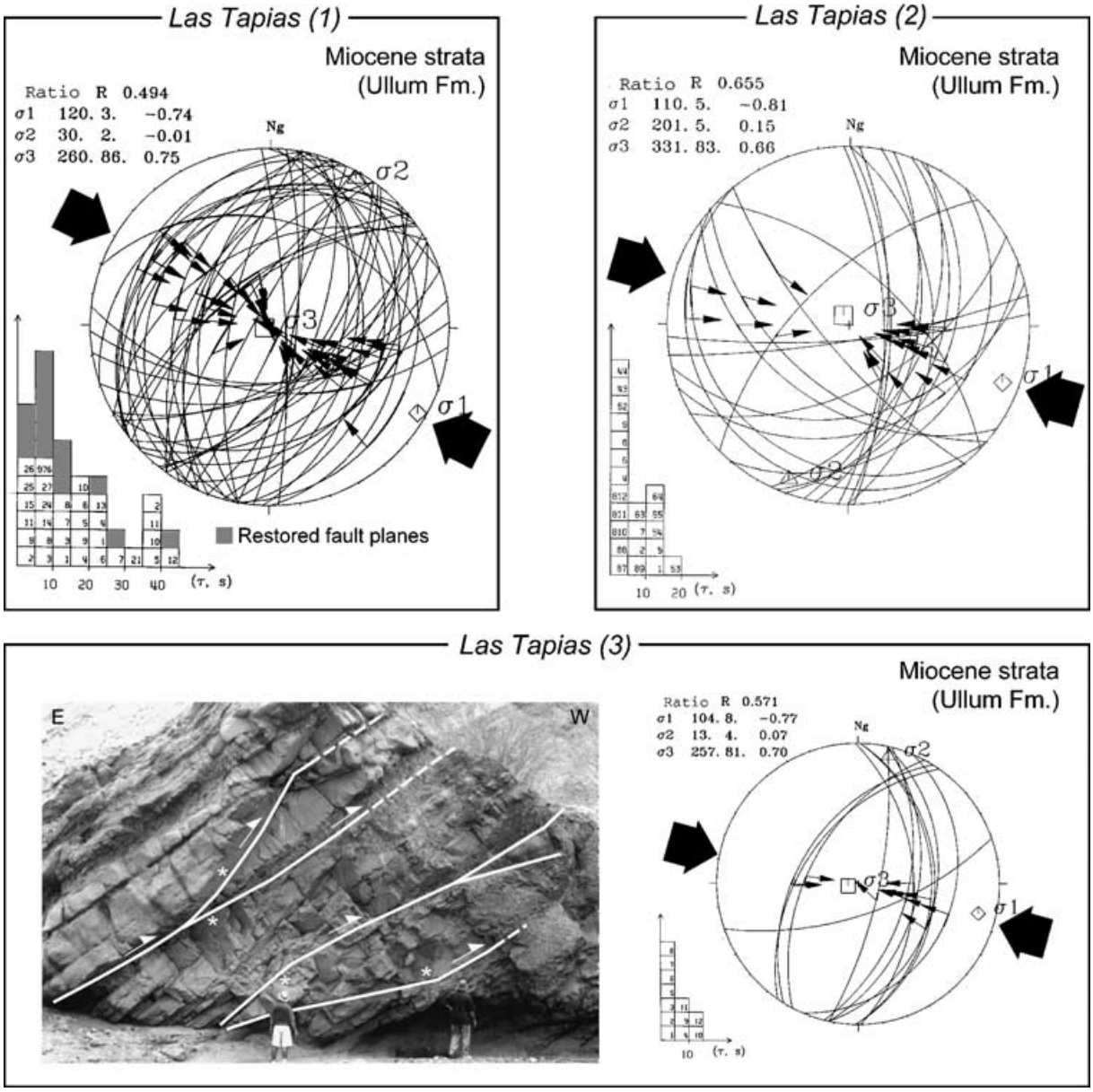

Figure 6. Lower-hemisphere stereoplots showing reverse-faulting data from the Lomas de las Tapias area (individual sites are located in Fig. 3 and listed in Table 1) together with results determined by the inversion method of Carey (1979). Inversions of fault slip data sets yield consistent results for state of stress in the Lomas de las Tapias area. They indicate a reverse-faulting stress regime with s_1 axis trending roughly N110°E. *Las Tapias* no 1: early fault planes, restored taking into account the stratification (N32°E 90°), was added for inversion and show that the computed stress regime is relatively stable during folding (see also Fig. 6). *Las Tapias* no 2: inversion results for fault-slip data measured in Miocene strata located in the fault zone. *Las Tapias* no 3: photograph illustrates the deformation style of the Neogene strata in Loma de las Tapias area (stars indicate where fault-slip data have been measured).

faults of southern Sierra de Villicúm and northern Sierra Chica de Zonda, this fault corresponds to bedding-slip faulting (Fig. 8). The degraded La Laja cumulative scarp has been reactivated during the $M_s = 7.4$, 1944, earthquake (INPRES 1982), producing a 6 km long surface rupture with 60 cm of maximum vertical slip at the surface (Castellanos 1945; Groeber 1944). Reverse slip-fault data measured on the excavated fault plane yields a N111°E-trending compressional stress axis consistent with the N107°E-trending σ_1-axis calculated by Régnier *et al.* (1992) from the crustal seismicity below Sierra Pie de Palo.

Inversion of fault kinematics on fault planes measured along the Quaternary segment of the Villicúm–Pedernal thrust provides constraints on the stress regime acting during the deformation of the Eastern Precordillera at ∼31°30′S latitude. Even though fault-slip data have mainly been measured on fault planes affecting Paleozoic and Neogene foreland strata, the stress regime computed at each site can be related to the eastward thrusting of the Eastern Precordillera. Further north, between 30°S and 31°S latitude, the initiation of deformation within the Eastern Precordillera is constrained by growth strata analyses and magnetostratigraphic studies and is dated at ∼2.7 Ma (Jordan *et al.* 1993; Zapata & Allmendinger 1996a,b). At these latitudes, the Eastern Precordillera is mainly characterized by blind thrusting and fault propagation folds. Between 31°S and 32°20′S latitude, the more developed relief of Eastern Precordillera suggests either an older initiation or a higher displacement rate.

Fault-slip data analysis along the Villicúm–Pedernal thrust thus shows that the Plio-Quaternary development of the Eastern Precordillera is dominated during initiation of folding, shortening and westward thrusting with a mean N110° ± 10°E-trending compressional stress axis (σ_1) (Table 1). Taking into account the N20°E-trending of Eastern Precordillera, it appears that the σ_1-axis is nearly perpendicular to the strike of the northern segment of the Villicúm–Pedernal thrust. This suggests that σ_1-axis is re-oriented with respect to the N80°E convergence between Nazca and South American plates.

3.3 Las Tapias segment

3.3.1 Geomorphic study

The Las Tapias fault (LTF) offers the opportunity to study the recent history of Eastern Precordillera at ∼31°30′S. In the low-lying region between Sierra de Villicúm and Sierra Chica de Zonda, the LTF forms west-facing, ∼10 m high discontinuous and degraded scarps that affect Quaternary alluvial sediments. The clastic source for alluvial material is the relief of Loma de Ullúm, and the stream flow direction is roughly SW–NE (Fig. 3). The piedmont has a well-preserved surface morphology with bars and swales formed by slightly varnished abraded boulders and subangular cobbles. It is still active as suggested by a well-developed network of braided streambeds incised ∼0.5 m into it. In further discussions, this alluvial surface will be referred to as A1.

The scarps are west-facing, which leads to pounding on the footwall of clastic deposits transported from Loma de Ullúm. Streambeds drain across the scarps from east to west. Thrust scarps grow against the main drainage. Nevertheless, the interaction of alluvial cutting and recurrent surface faulting has generated a strath terrace sequence that records the faulting history on the hanging wall. As the stream gradients are relatively high (<8°), recurrent faulting on the LTF has raised the hanging wall sufficiently resulting in significant downcutting. This stream incision into the upthrown block has created A2 and A3 terraces that end abruptly at the fault scarp (Fig. 3). Both surface morphologies of A2 and A3 are marked by the absence of bars and swales and by the occurrence of well-developed desert pavements. Moreover, although the outcrop conditions are fairly good, no significant difference in weathering has been observed between A2 and A3 surfaces. Nevertheless, on aerial photographs, A2 and A3 can be easily distinguished by their differential elevations, and by the differences in both the incision pattern and the degree at their surfaces. A3 is much more heavily incised by small gullies than A2, which is suggestive of an older surface. In an attempt to establish absolute ages for this stratigraphically based chronology between A1–A3, each surface has been sampled for cosmic ray exposure dating.

3.3.2 Cosmic ray exposure dating

The application of *in situ*-produced cosmogenic nuclides in quantitative geomorphology is based on their continuous production in the upper few metres of rocks exposed to cosmic rays. At a given site, the production is controlled by the location (i.e. latitude and altitude) and by the geometry exposure (i.e. the topography). At the surface and for any exposure duration, the largest cosmogenic accumulation corresponds to a flat surface that has experienced no erosion (Lal 1991; Nishiizumi *et al.* 1993). The ^{10}Be production rate depends on the energy-dependent production cross-section for reaction with the target atoms and on the cosmic ray flux entering the environment of the Earth (Lal & Peters 1967; Raisbeck et al. 1984). This latter parameter is influenced by the solar activity intensity (Bard & Broecker 1992), but depends mainly on the strength of the magnetic field of the Earth (Robinson *et al.* 1995). This effect, together with dissipation in the atmosphere accounts for the observed altitudinal and latitudinal variability in the production rate. Over the past ten years, altitudinal and latitudinal production rate variations have been modelled using empirical polynomials (e.g. Lal 1991; Dunai 2000; Stone 2000). In this study, Stone (2000) polynomials have been privileged since they allow one to take into account the physical properties of cosmic ray propagation in matter, using the atmospheric pressure as a function of altitude. In the upper few metres of the surface of the Earth, *in situ* production of ^{10}Be within exposed rocks is primarily caused by neutron-induced spallation of O and Si. Nevertheless, a small proportion of ^{10}Be is also produced by stopping negative muons (Lal 1991). Production rates for the muon and neutron components were thus scaled with altitude and latitude using the recasting of the Lal (1991) formulation as described by Stone (2000).

Measurements of cosmogenic ^{10}Be ($t_{1/2} = 1.5$ Myr) concentrations within the quartz mineral fraction of surficial rocks on abandoned alluvial features in semi-arid climatic conditions have been demonstrated to be particularly well-suited for dating deformed geomorphic features (Ritz *et al.* 1995; Siame *et al.* 1997a,b; Brown *et al.* 1998). The build-up of ^{10}Be in that mineral fraction does not suffer from loss by diffusion and its radiogenic formation is negligible within quartz minerals (Sharma & Middleton 1989). The *in situ*-produced ^{10}Be nuclide thus accumulates with time until its concentration reaches a steady-state balance between production and loss by erosion and radioactive decay. The ^{10}Be content of a given surficial boulder reflects the entire exposure history of the surface and integrates the exposure in the source region during transport and the exposure since abandonment in its current position. Assuming that (1) the erosion–sedimentation processes are sufficiently rapid for little accumulation to occur before or during the emplacement of the boulders, and (2) little loss of ^{10}Be caused by erosion occurred after the surface abandonment, the ^{10}Be content in surficial rocks is directly related to the period post-dating surface abandonment. Sampling has been limited to the largest boulders of quartz-rich rocks embedded on local flat-topped areas to minimize the effects of exposure prior to deposition. The second assumption is supported not only by the arid climatic conditions of the study region, but also by field observations of dark desert varnish developed on surficial boulders and cobbles.

The ^{10}Be concentration C (atom g^{-1}) within a surficial embedded boulder as a function of time t (yr) is given by

$$C(t) = C(0)\,\mathrm{e}^{-\lambda t} + \frac{P_\mathrm{n} P_0}{\varepsilon\rho/\Lambda_\mathrm{n} + \lambda}\left\{1 - \exp\left[-\left(\varepsilon\frac{\rho}{\Lambda_\mathrm{n}} + \lambda\right)t\right]\right\} + \frac{P_\mu P_0}{\varepsilon\rho/\Lambda_\mu + \lambda}\left\{1 - \exp\left[-\left(\varepsilon\frac{\rho}{\Lambda_\mu} + \lambda\right)t\right]\right\}, \quad (1)$$

where ε is a mass erosion rate (g cm^{-2} yr^{-1}), P_0 is the local production rate (atom g^{-1} yr^{-1}) corrected according to Stone (2000), P_n and P_μ are the neutron and muon contribution to the total production rate, respectively (where $P_\mu = 0.015$ and $P_\mathrm{n} + P_\mu = 1$, e.g. Brown *et al.* 1995), ρ is the rock density (g cm^{-3}), Λ_n (∼150 g cm^2) and Λ_μ (∼1300 g cm^2) are the attenuation lengths of neutrons and muons, respectively (e.g. Brown *et al.* 1992), λ is the radioactive decay constant (yr^{-1}) and C (0) is the cosmogenic nuclide concentration at the initiation of the present surface exposure episode. This

equation assumes constant rates of production and erosion and has two unknowns: ε and t. To calculate a surface exposure lower limit from this equation, one must check that exposure prior to the present exposure episode was minimal and assume that the mass erosion rate is negligible. In a previous study dealing with cosmic ray exposure dating, we demonstrated that the impact of erosion can be ignored in this part of the Andean foreland of Western Argentina where arid climatic conditions prevail (Siame *et al.* 1997a).

Large 20–30 cm rhyolitic boulders were crushed, then sieved (0.25–1.0 mm) and selectively etched in H_2SiF_6, HCl and HF in order to eliminate all mineral phases except quartz and potential surface contamination by ^{10}Be produced in the atmosphere. The cleaned quartz was then completely dissolved in HF. After addition of 300 μg of ^{9}Be carrier, targets of purified beryllium were then prepared for accelerator mass spectrometry (AMS) analysis. To obtain the rates of surface production at each sampling location, we use the best-fitting calibrated high-latitude sea level production rate of 5.1 ± 0.3 atom g^{-1} quartz yr (Stone 2000) corrected for altitude and elevation using the correction factors of Stone (2000) (Table 2). Assuming that the geomagnetic latitude over the exposure lifetime of the terraces averages out to the current geographic latitude, we do not attempt to correct the rate of ^{10}Be production for variations in the intensity of the magnetic field. Thus, all of our dates are given in ^{10}Be yr and allow straightforward correction for future refinements in production rate histories.

The rocks sampled on the lower surface (A1) have minimum CRE ages of 1.1 (±0.3), 1.4 (±0.6) and 1.9 (±0.8) ^{10}Be kyr that are in close agreement with the geomorphic observations, indicating that the A1 surface is recent. As the source material is very local, exposure prior to deposition on to the alluvial surface can reasonably be considered to be minimal (Table 2). Thus, for further discussions, we calculated an A1 mean minimum CRE age of 1.5 (±0.8) ^{10}Be kyr. The two boulders sampled on the intermediate surface (A2) have minimum CRE ages of 5.3 (±0.7) and 6.8 (±1.0) ^{10}Be kyr, respectively. The two boulders sampled on the upper surface (A3) have minimum CRE ages of 18.0 (±2.3) and 18.7 (±2.3) ^{10}Be kyr, respectively. Despite a limited sampling of each surface, the CRE ages obtained for each surface are in close agreement, and errors are small relative to the age difference between surfaces. This suggests strongly that post-depositional processes have not been acting intensively on the flat-topped areas of sampling. Even though neglected, post-depositional processes are most probably not uniform across abandoned surfaces (Brook & Kurz 1993). Taking into account the uncertainties associated with the CRE ages calculated for both A2 and A3 samples, the ^{10}Be contents for A2 and A3 samples yield the same CRE ages (Table 2). The oldest ages will thus be considered as the best approximation for the actual age of abandonment, that is, 6.8 (±1.0) and 18.7 (±2.3) ^{10}Be kyr for the A2 and the A3 surfaces, respectively.

3.3.3 *Vertical displacements and uplift rate*

The geometry of the displaced alluvial deposits with respect to the fault scarps has been studied to estimate the uplift rate for the hanging wall of the LTF. Indeed, A2 and A3 fill terraces result from episodic fault incision into the upthrown block of the LTF. The vertical separation between the projection of these terraces measured at the inferred fault plane may thus provide a first approximation of the vertical component of fault displacement. To constrain the vertical component of fault displacement, three topographic profiles have been surveyed perpendicular to the fault trace (Fig. 8). Although scarps appear to be relatively well preserved, scarp heights have only been measured on broad crests between the gullies that cut into the relief, to minimize the effect of local erosion on such steep slopes. The vertical scarp heights derived from topographic profiles no 1 and 2 are relatively well constrained. Profile no 1 shows that the surface of the upper terrace (A3) is 11 ± 1 m above the surface of the alluvial unit that skirts the toe of the scarp (A1). Profile no 2 indicates that the surface of the intermediate terrace (A2) is 6 ± 2 m above the surface of the alluvial unit A1 (Fig. 8). Profiles no 1 and no 2 can be regarded as compound fault scarps, that is scarps produced by more than one rupture event. In the case of compound scarps, nickpoints are expected on scarp faces caused by rejuvenation of the scarps by successive rupture events. Unfortunately, the scarp faces appear to be like wide planar slopes with angle of ∼25°. This observation suggests strongly a high-slip rate (short recurrence time), frequent rejuvenation of the scarp and associated slope regrading then destroying earlier nickpoints. A N110°E projection of the topographic profiles shows that the face of the scarp bounding A3 has retreated eastwardly by ∼5 m with respect to the face of the scarp bounding A2. Moreover, the 11 (±1) m high scarp is bounded at its toe by an active streambed, which has washed away the material.

North of profile no 2, the fault trace disappears where a large streambed incised the scarps (Fig. 8). Nevertheless, anomalous slopes that are opposite to the regional NW–SE sense of drainage can be observed between active braided streambeds incised into the A1 surface. Moreover, in this area, stream incision is higher downslope, by ∼50 cm, than upslope. In fact, topographic profile no 3 reveals a small upstream warp corresponding to a 60 cm high,

Table 2. *In situ*-produced ^{10}Be concentrations and minimum CRE ages of samples from the three alluvial units affected by the Las Tapias fault. Measurements of ^{10}Be were undertaken at the Tandétron AMS Facility at Gif-sur-Yvette, France (Raisbeck *et al.* 1987; 1994), using NIST ^{10}Be standard (Standard Reference Material nos 43–25, ^{10}Be/^{9}Be = 2.68×10^{-11}, 1986 August). For each sample, the analytical uncertainty associated with the ^{10}Be concentration results from uncertainties based on counting statistics (1σ), conservative assumptions of 5 per cent variability in Tandétron response, and a 50 per cent uncertainty in the chemical blanks correction. The uncertainty on the minimum CRE ages includes the analytical uncertainty plus an assumed 10 per cent error associated with the calibrated sea level high-latitude value of 5.1 ± 0.3 atom ^{10}Be g^{-1} quartz yr (Stone 2000).

Sample	Surface	Site		Scaling factors (Stone 2000)				P_0 (at g^{-1} yr^{-1})	[Be-10] (at g^{-1})	[Be-10] error (at g^{-1})	T_{min} (yr)	T_{min} error (yr)
		(°S lat)	Z (m)	$P(Z)$ (hpa)	$S\lambda[P(Z)]$	$M_\lambda[P(Z)]$	$F_\lambda[P(Z)]$					
LS96-013	A1	31.41	890	910.78	1.695	1.294	1.684	8.6	1.24E + 04	4.98E + 03	1 444	586
LS96-007	A1	31.41	890	910.78	1.695	1.294	1.684	8.6	9.22E + 03	2.62E + 03	1 074	312
LS96-008	A1	31.41	890	910.78	1.695	1.294	1.684	8.6	1.60E + 04	7.00E + 03	1 861	824
LS96-009	A2	31.41	905	909.13	1.714	1.303	1.703	8.7	4.61E + 04	5.92E + 03	5 310	753
LS96-010	A2	31.41	900	909.68	1.708	1.300	1.697	8.6	5.92E + 04	7.94E + 03	6 848	1006
LS96-011	A3	31.41	910	909.58	1.720	1.305	1.710	8.7	1.56E + 05	1.75E + 04	17 975	2283
LS96-012	A3	31.41	915	908.03	1.727	1.308	1.716	8.8	1.63E + 05	1.72E + 04	18 687	2274

Table 3. Estimation of the uplift rate on the LTF using height and CRE age differences between the A3, A2 and A1 surfaces. Uncertainties in the estimations of uplift rate are given according to the division rule for values with no equal standard deviations, i.e. $U \pm \sigma_u = (H/A) \pm U\sqrt{(\sigma_A/A)^2 + (\sigma_H/H)^2}$.

	A1/A2	A1/A3	A2/A3
Height difference (H, m)	6 ± 2	11 ± 1	5 ± 2
Age difference (A, ka)	5 ± 1	17 ± 2	12 ± 3
Uplift rate (U, mm yr^{-1})	1.1 ± 0.5	0.6 ± 0.1	0.4 ± 0.2
Mean uplift rate (mm yr^{-1})	0.7 ± 0.3		

west-facing slope that may be interpreted as the degraded trace of the most recent event on the fault (Fig. 8). As this upslope-facing warping is antithetic respect to the drainage slope, it can hardly be interpreted as a depositional feature at the top of a strath terrace. As these anomalous drainage patterns are located on A1 surface, between the active streambeds, the most recent event cannot be dated more accurately than being younger than the age of the A1 surface, that is 1.5 ($\pm$0.8) ^{10}Be kyr.

The scarps bounding the A2 and A3 terraces have been constructed through time by repeated faulting on the LTF. Since, topographic profiles provide constraints on minimum vertical displacement between A3, A2 and A1 and ^{10}Be CRE ages provide lower limits for the time elapsed since surface abandonment, these data allow one to estimate lower limits for the long-term uplift rate (Fig. 9 and Table 3). An offset of 11 ($\pm$1) m between the A3 and A1 surfaces and an age difference of roughly 17 ($\pm$2) kyr yield an uplift rate of $\sim$0.6 ($\pm$0.1) mm yr^{-1} (Table 3). The data obtained for A2 and A1 yield to an uplift rate of $\sim$1.1 ($\pm$0.5) mm yr^{-1}, which is not significantly different (Table 3). Because A2 terrace has been inset into the A3 terrace, a third estimation can be calculated using the 5 ($\pm$2) m height difference between A2 and A3. It yields an uplift rate of $\sim$0.4 ($\pm$0.2) mm yr^{-1}, which is in close agreement with the previous estimates (Table 3). All together, these estimates yield a mean uplift rate of 0.7 ($\pm$0.3) mm yr^{-1} (Fig. 9).

3.3.4 Shortening rate estimates

To calculate a shortening rate (S) on a reverse fault, one can take into account the rate of vertical displacement (V), the dip of the fault (P), and the direction of shortening on the fault (pitch of the striae, *pi*) using

$$S = \frac{V}{(\tan(pi)\cos(90 - P)}. \quad (2)$$

A 0.7 ($\pm$0.3) mm yr^{-1} uplift rate have been calculated for the LTF. The topographic profiles provide only 'apparent' vertical displacements. They allow the height between the uplifted alluvial surfaces and the surface of the alluvial unit that skirts the toe of the scarps to be measured. In fact, on the footwall block, units A2 and A3 are most probably buried under the A1 unit, and to estimate the actual vertical displacements, one should be able to take into account the thickness of the alluvial units. Thus, to calculate a lower limit for the shortening rate, the 0.7 ($\pm$0.3) mm yr^{-1} uplift rate has been used as a proxy for the rate of vertical displacement.

Though a relatively linear trace, the LTF curves slightly eastward where it crosses the lowest terrains, such as streambeds cross-cutting the scarps, and curves westward where it crosses the highest terrains (Fig. 3). These observations suggest that the thrust plane located beneath the edge of the Eastern Precordillera has reached the surface as a relatively high-angle east-dipping single fault (Fig. 3). The stress regime determined by quantitative inversions of fault-slip data sets indicates that the LTF is a purely reverse fault, and most of the major fault planes studied within the LTF area are characterized by eastward dips ranging between 45° and 75°. The theoretical pitch of the striae in the fault plane can be calculated using the regional N110°E-trending σ_1 compressional axis projected into an idealized N20°E-trending fault plane dipping 60° ($\pm$15°) towards the east (Table 4). Combined with the previously estimated minimum uplift rate, these estimations of fault dip and pitch of the striae yield a shortening rate of $\sim$0.8 ($\pm$0.5) mm yr^{-1}. Taking into account the estimated vertical and horizontal slip rates, the Las Tapias segment can be regarded as a relatively fast active reverse fault, which is consistent with the observation of planar-faced scarps.

Table 4. Estimation of the shortening rate on the LTF as a function of dip and theoretical pitch. Theoretical pitches have been computed using the N110°E-trending σ_1 compressional stress axis applied on N20°-striking idealized fault planes dipping 60°($\pm$15°) towards the east. The shortening rates (S) are calculated using $S = \frac{U}{(\tan(pi)\cos(90-P)}$ with U, the mean uplift rate (mm yr^{-1}) used as a proxy for the vertical rate of displacement, *pi,* the theoretical pitch, and P, the dip of the fault near the surface. Uncertainty in the estimation of shortening rate is based on the propagated uncertainties using the division rule for values with no equal standard deviations (e.g. Table 3).

Fault dip (P, degree)	Theoretical pitch (Pi, degree)	Uplift rate (mm yr^{-1})	Shortening rate (mm yr^{-1})
60 ± 15	84 ± 2	0.7 ± 0.3	0.8 ± 0.5

4 SHORTENING RATE FROM THE SEISMIC MOMENT SUM

Earthquake moment tensor sums can be used to calculate shortening rates caused by seismic deformation (Jackson & McKenzie 1988; Jost & Herrmann 1989; Ego *et al.* 1995; Molnar & Ghose 2000). The rate of crustal shortening calculated by summing the seismic moments of earthquakes may be compared with the slip rates determined using CRE dating of displaced landforms. The seismic moment is defined as

$$M_0 = \mu A u \quad (3)$$

(Aki 1966; Hanks & Kanamori 1979), where M_0 is the scalar seismic moment, μ is the shear modulus ($\sim 3 \times 10^{11}$ dyne cm^{-3}, e.g. Aki 1966; DePolo & Slemmons 1990), A is the surface area of the fault and u is the average coseismic displacement. The cumulative slip on a fault can be estimated by summing the seismic moments of earthquakes causing slip on the fault (e.g. Brune 1968; Davis & Brune 1971). However, in the San Juan region, seismic energy is not released on a single fault but on fault planes with orientations distributed over a seismogenic volume. In such a case, Kostrov's (1974) methodology is more suitable as it uses the seismic moment tensors to calculate the strain resulting from seismic slip of all the faults in the region. The seismic moment tensor for a single rupture event may be expressed as

$$M_{ij} = \mu A(u_i v_j + u_j v_i), \quad (4)$$

where v_i are the direction cosines of the vectors normal to the nodal plane and u_i is the average slip in vectorial form (Aki & Richards 1980; Ben-Menahem & Singh 1981). The principal values of the moment tensor $-M_0$, 0 and $+M_0$, correspond to the P, B and T axes of the fault plane solution (Gilbert 1970; Súarez *et al.* 1983). Following Kostrov's (1974) method, the mean rate of irrotational

strain ($\dot{\varepsilon}_{ij}$) in a volume V over a period of time t caused by slip on N different faults located within that volume is given by

$$\dot{\varepsilon}_{ij} = \frac{1}{2\mu V t} \sum_{n=1}^{N} M_{ij}^{n}. \quad (5)$$

The principal directions of the strain rate are calculated by diagonalizing $\dot{\varepsilon}_{ij}$. The crustal shortening rate is thus calculated by multiplying the horizontal component of the maximum compressive strain rate ($\dot{\varepsilon}_{ij} H_{\max}$) times the width of the deformed volume in the direction of $\dot{\varepsilon}_{ij} H_{\max}$ (e.g. Súarez *et al.* 1983). In eq. (5), the member $\sum_{n=1}^{N} M_{ij}^{n}$ represents the seismic moment sum. The methodology used to calculate this seismic moment sum is fully described in Jost & Herrmann (1989).

In the San Juan Province, 12 shallow focal mechanism solutions (essentially the $M_w = 7.4$, 1977 Caucete event) have been recorded over the last 23 yr. These seismic events are located in a 45 × 100 km^2 zone between the Sierra Pie de Palo and Sierra Valle Fértil (Fig. 2), with a seismogenic depth of ∼30 km (Table 5). Within this particular volume the $\dot{\varepsilon}_{ij} H_{\max}$ value is 6.45×10^{-9} yr^{-1} and is oriented N93°E (Table 5). This orientation is consistent with the N110° (±10°)E-trending σ_1 compressive axis determined from fault slip kinematics. Following the methodology defined by Súarez *et al.* (1983), a 3 mm yr^{-1} rate of crustal deformation is calculated by multiplying the $\dot{\varepsilon}_{ij} H_{\max}$ value times the width of the deformed area (45 km), measured in the direction of $\dot{\varepsilon}_{ij} H_{\max}$ (N93°E) (Table 5). This estimation is a lower bound since fault creep, viscoelasticity deformation and contribution caused by earthquakes with magnitudes smaller than $M_w = 5.3$ are neglected. Even if the seismic moment sum used is strongly dependent on the time window, it is striking that the shortening rate in the Sierra Pie de Palo caused by seismic deformation determined over 23 yr is three times greater but of the same order of magnitude as the rate that is determined over ∼20 kyr using CRE dating. Thus the LTF appears as one of the major ramps of the Eastern Precordillera west-verging thrust system. The shortening rate determined using the seismic moment sum is obviously dominated by the 1977 Caucete event. Even if one argued as to the degree to which the available time window is representative, the San Juan region has experienced four earthquakes with $M \approx 7$ during the previous 60 yr. Thus, considering one $\approx$ 7 event in 23 yr seems realistic to address the seismic strain released in the San Juan region during the second half of the 20th century.

5 SEISMIC HAZARD ASSESSMENTS

In the San Juan city area, previous seismic hazard studies have focused mainly on small surface ruptures distributed on the eastern flank of the Eastern Precordillera, such as the La Laja fault (Figs 1 and 7) (INPRES 1982). Trenches and paleosoil dating have revealed that the recurrence interval of these small active faults should be greater than several thousand years (INPRES 1982). Even if they are associated with small scarps, none of those small surface ruptures present either the conspicuous geomorphic characteristics or the cumulative displacement of the Las Tapias and Villicúm segments. In fact, folding of Neogene sediment sequences on the Eastern Precordillera fold limb is most probably accompanied by slip along bedding planes. This slip generates flexural slip faults that are rooted in the eastern limb of the Eastern Precordillera. During an earthquake, intersection of flexure-slip faults with the surface may locate scarps and produce fault-line features. Nevertheless, these small surface ruptures should be regarded as being secondary fractures formed either by ground shaking or more probably by flexural slip on bedding planes (see Fig. 7: the fault plane at La Laja is strictly parallel to the Neogene bedding planes).

Table 5. Seismic moment sum. (a) List of the focal mechanism solutions used for the calculation. (b) Numerical results for the calculation of the regional deformation rate caused by seismic contribution.

(a) Focal mechanism solutions

Date	Lat (°S)	Lon (°W)	Depth (km)	NP1		NP2		*T* axis		M_0 (dyn cm)	M_w
				Strike	Dip	Strike	Dip	Plunge	Azimuth		
77/11/23	31.22	67.69	20.8	183	44	4	46	89	289	1.86×10^{27}	7.4
77/11/24	31.53	68.05	46.5	190	34	8	56	79	275	2.81×10^{24}	5.6
77/11/28	32.02	68.21	33.1	150	52	43	69	43	0	2.84×10^{24}	5.6
77/11/28	31.67	67.64	15.0	182	21	345	70	64	246	2.02×10^{25}	6.1
77/12/06	31.43	68.11	19.0	181	37	11	54	80	306	7.95×10^{25}	6.9
77/12/10	31.28	68.03	34.9	199	29	348	65	67	232	1.92×10^{24}	5.5
78/01/17	31.53	68.08	23.0	142	66	47	79	25	2	1.07×10^{25}	6.0
78/08/21	31.79	68.11	25.0	218	9	49	81	54	321	1.16×10^{24}	5.3
79/08/30	31.40	67.06	27.0	354	31	233	73	55	176	2.03×10^{24}	5.5
80/04/09	31.49	67.42	15.0	340	37	108	65	336	59	1.28×10^{24}	5.3
80/11/10	31.52	67.55	15.0	133	31	358	67	62	301	3.60×10^{24}	5.6
86/08/11	31.19	67.76	26.5	187	49	285	80	35	155	1.33×10^{24}	5.4

(b) Seismic contribution to the regional deformation rate

P			*B*			*T*		
Value (dyn cm)	Azimuth	Plunge	Value (dyn cm)	Azimuth	Plunge	Value (dyn cm)	Azimuth	Plunge
-1.9×10^{27}	N93°E	1.3	9.6×10^{24}	N183°E	0.5	2×10^{28}	N295°E	88.6

Seismic moment sum value: 1.90×10^{27} dyn cm.
Deformed volume: $45 \times 100 \times 30$ km^3.
$\dot{\varepsilon}_{ij} H_{\max} = 6.47 \times 10^{-7}$ yr^{-1}.
Shortening rate = 3 mm yr^{-1}.

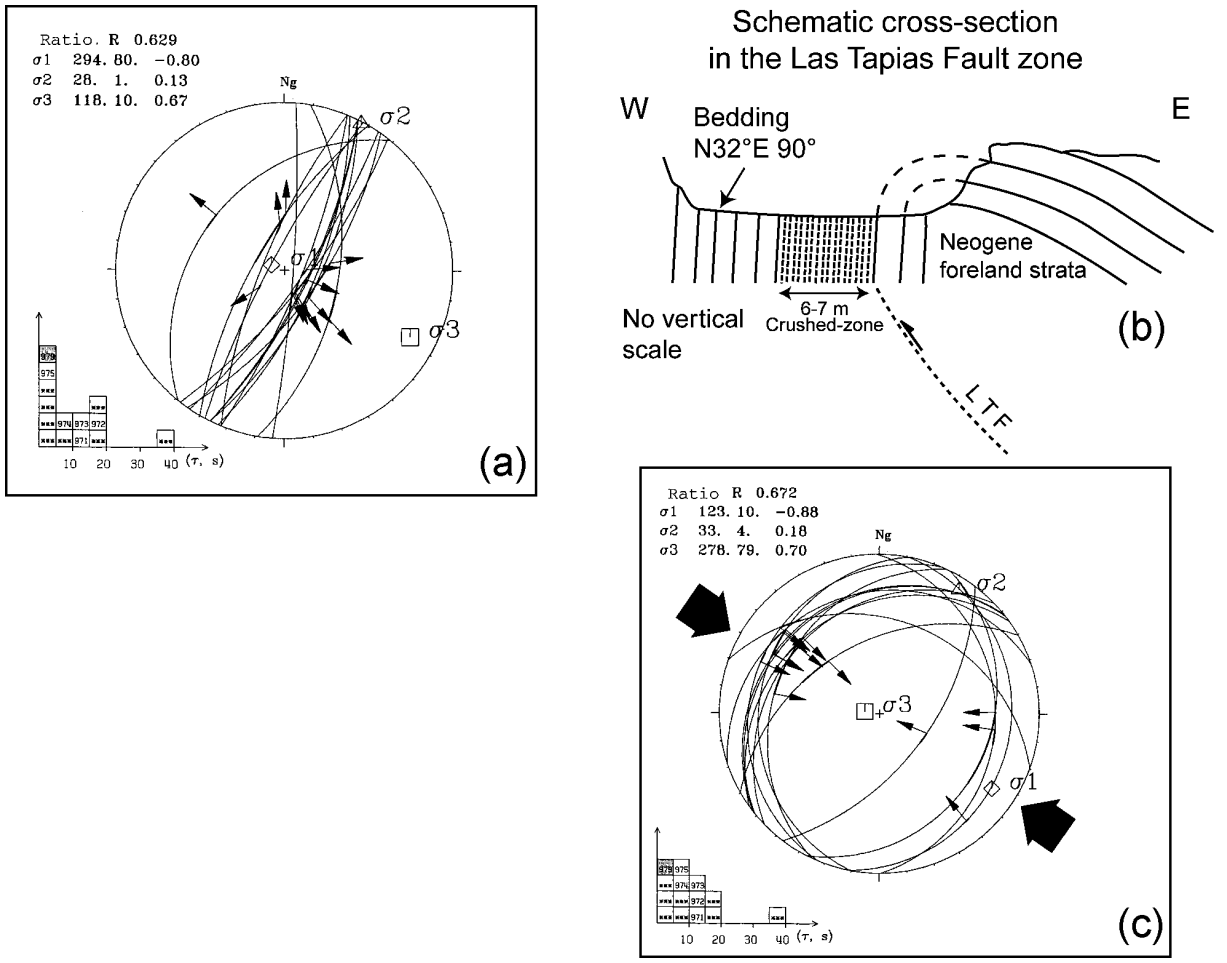

Figure 7. (A) Lower-hemisphere stereoplot showing apparently normal-slip faulting observed at *Las Tapias* no 1. These apparently normal faults are localized in the crushed-zone where the stratification is vertical (cross-section B). (C) Lower-hemisphere stereoplot showing restoration of the normal-slip faulting taking into account the measured stratification showing a reverse stress regime very similar with the one determined in the area. This apparently normal faulting most probably correspond to early bedding-slip faulting that have been rotated during folding.

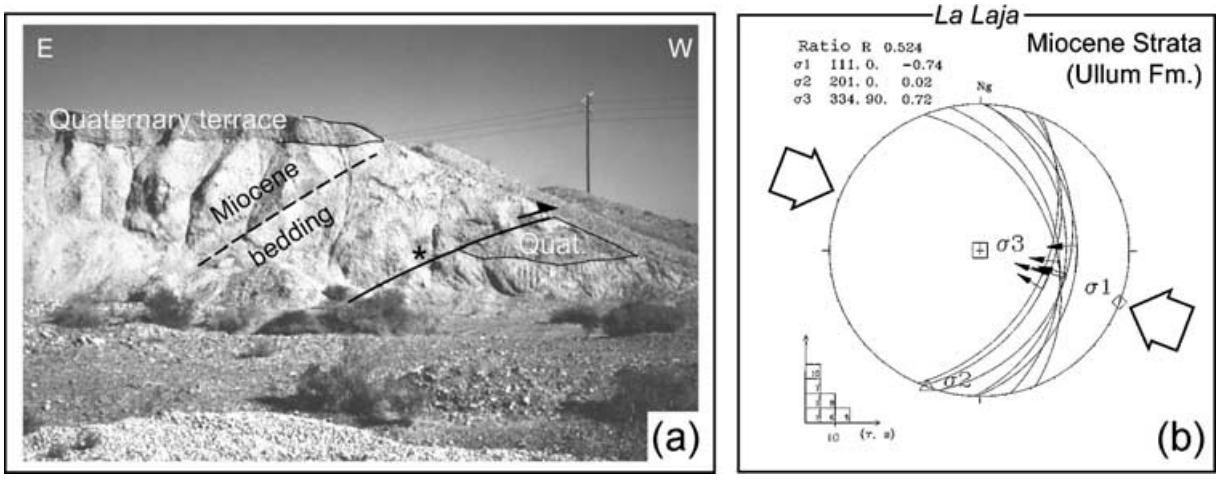

Figure 8. (A) E–W photograph of the La Laja fault, which have been reactivated during the $M_s = 7.4$ seismic event that damaged San Juan in 1944. This 6 km long active reverse structure is localized on eastern piedmont of the Sierra de Villicum range and presents a compound scarp. It affects the same Neogene foreland strata as the Las Tapias fault. The fault is parallel to the Neogene stratification (bedding-slip faulting). (B) Lower-hemisphere stereoplot showing reverse-slip faulting data measured using striations observed on an excavated fault plane (the star on the photograph locates measurements). The stress regime is computed from this poorly distributed slip-fault set assuming the additional hypothesis that the σ_3-axis is vertical (open arrows outside the stereoplot). It is consistent with the regional state of stress in the Loma de las Tapias area (e.g. inversion results in Fig. 6), suggesting the stability of the stress regime during the ongoing deformation.

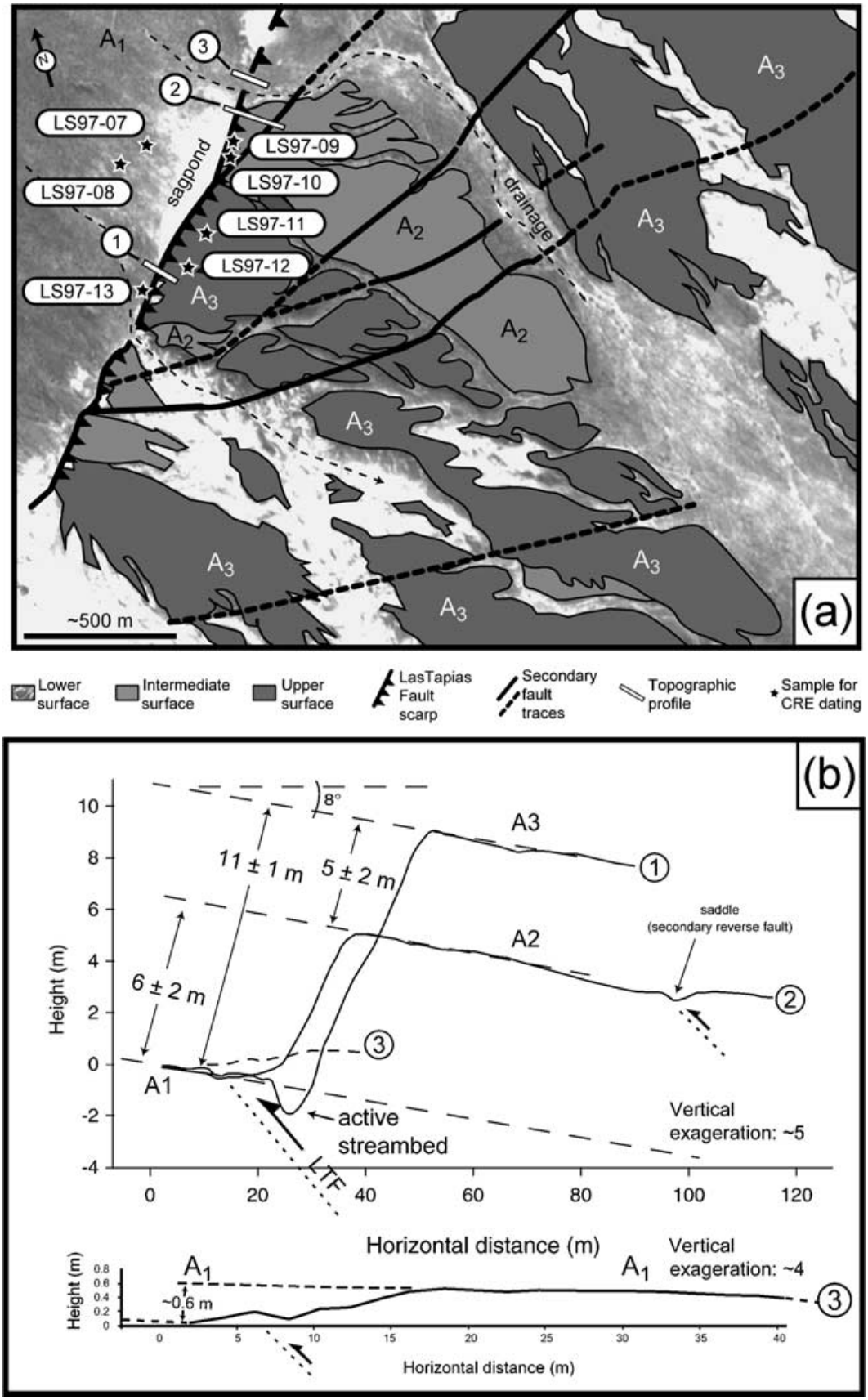

Figure 9. (A) Map of the alluvial deposits affected by the Las Tapias fault based on both stratigraphy and surficial morphology observed in the field and on the aerial photograph (located in Fig. 3). (B) N110°E-striking topographic profiles constructed perpendicularly to the Las Tapias scarps (circled numbers refer to locations on A).

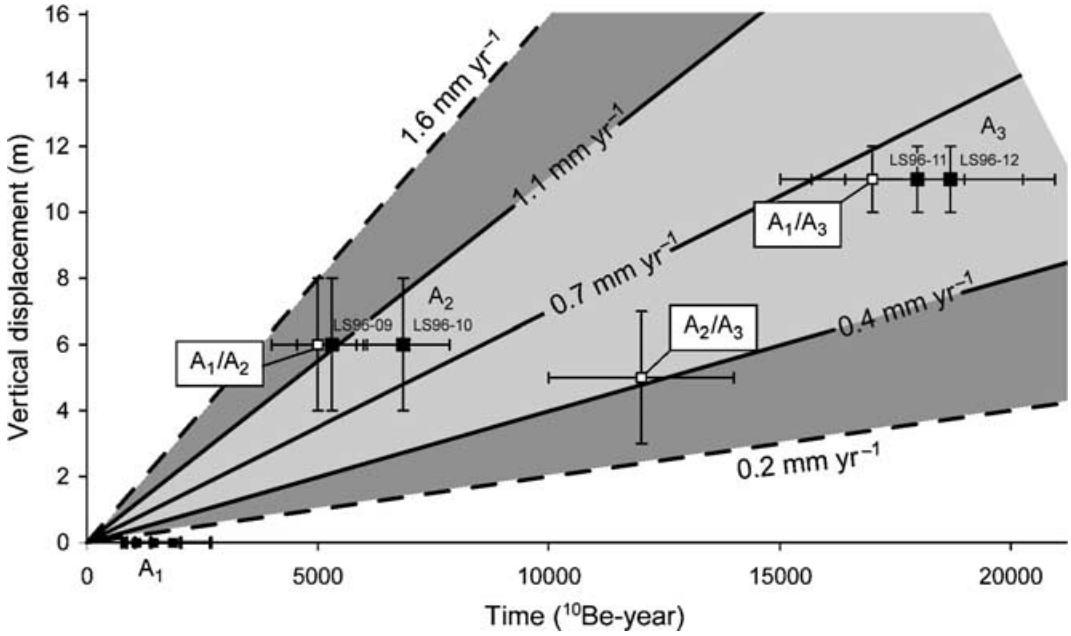

Figure 10. Uplift rate estimates from vertical displacements and cosmic ray exposure dating. Thick lines and the light grey area show the uplift rate estimate and the associated uncertainties (e.g. Table 3). Thick dashed lines and the dark grey area show upper and lower limits of uplift rate (e.g. Table 3). Keys: dark squares, dated surfaces; open squares, vertical and age difference between the dated surfaces.

In order to improve earthquake source characterization and seismic hazard assessments in the San Juan city area, the maximum expected earthquake magnitude and recurrence intervals have been estimated for the Villicúm–Pedernal thrust segments. Indeed, possible rupture segments may be reflected by the structural discontinuities of the thrust zone, especially at the end of overlapping imbricate faults. Thus, the structural segmentation described previously is used as a basis for seismic hazard assessments at the level of individual thrust segments, assuming that they may behave independently. This assumption is supported by the fact that, in such imbricated thrust systems, most historic worldwide earthquakes have involved rupture on one thrust fault while others have remained quiet (e.g. Carver & McCalpin 1996). Two methods have been used: the rupture area method, based on statistical relationships (Wells & Coppersmith 1994), and the moment magnitude method, based on scaling laws (Brune 1968; Hanks & Kanamori 1979; Kanamori 1983).

5.1 Rupture area method

This method uses empirical correlation between historic earthquake magnitudes and rupture areas. The approach of Wells & Coppersmith (1994) is based on 244 worldwide earthquakes, with magnitudes ranging between 4.3 and 8.3. For reverse faults, the relationships of Wells & Coppersmith (1994) correlate poorly the surface rupture length (L) with the coseismic displacement (D). This is mainly because of the fact that small amounts of coseismic displacement are generally observed for thrust-fault-generated earthquakes. Thus, for paleoearthquakes that occurred on structures but did not produce a conspicuous surface rupture, the following relationship between rupture area (RA) and magnitude (M_w) is used:

$$M_w = 4.33 + 0.90 \log(RA). \tag{6}$$

However, in the absence of conspicuous evidence of surface rupture, it is somewhat difficult to decide whether the entire fault plane area, or only a portion of it, ruptured during a paleoearthquake. Thus, for each Villicúm–Pedernal thrust segment, the paleorupture area has been calculated by multiplying the inferred rupture length, based on the structural segment length, times the down-dip dimension of the fault, using a seismogenic depth of $\sim 25 \pm 5$ km (Smalley *et al.* 1993), and considering a fault dip ranging between 45° and 75° (Table 6).

A moment magnitude of ~7.6 is estimated for a maximum earthquake reactivating the entire length of the Villicúm–Pedernal thrust (Table 6). Nevertheless, as the Villicúm–Pedernal thrust is segmented, only one segment may have ruptured during a single event, yielding lower maximum magnitude estimates (Table 6). The Villicúm and Las Tapias segments are characterized by the most conspicuous traces within the Quaternary deposits. They may be regarded as the best seismic source candidates for paleoearthquake ruptures. The maximum moment magnitude expected for these segments are 7.2 and 6.8, respectively. Taking into account the fact that, for magnitudes under 7.5, surface-wave magnitudes are of the same order of magnitude as moment magnitudes, it is striking that the moment magnitude expected for a maximum earthquake reactivating both the Villicúm and the Las Tapias segments is close to $M_s = 7.4$ of the 1944 San Juan earthquake.

5.2 Seismic moment method

The seismic moment method gives the seismic moment (M_0, dyne cm) and moment magnitude (M_w) as a function of the rupture length (L), the seismogenic width (W) and the average coseismic displacement (AD) (Hanks & Kanamori 1979):

$$M_0 = \mu ADLW, \tag{7}$$

$$M_w = \frac{\log M_0 - 16.1}{1.5}, \tag{8}$$

where μ is the shear modulus. Using the previous estimations of M_w, one can estimate paleoseismic moments, and thus average

Table 6. Estimated seismic hazard parameters for a maximum earthquake reactivating the Villicúm–Pedernal segments from Wells & Coppersmith (1994) rupture area–magnitude statistical relationship (∗), and Hanks & Kanamori (1979) moment magnitude scaling law (∗∗).

Parameters	
Seismogenic depth (km) (Smalley *et al.* 1993)	25 ± 5
Fault dip (degree)	60 ± 15
Down dip width (km)	30 ± 7
Shortening rate (mm yr^{-1})	0.8 ± 0.5

Table 6. (*Continued*) Individual segments

Seismic hazard parameters	Villicum segment	Las Tapias segment	Zonda–Pedernal segment	Villicúm–Pedernal whole length	Only Villicúm–Las Tapias
Estimated rupture length (km)	47	18	80	145	65
Rupture area (RA km^2)	1410 ± 320	540 ± 120	2400 ± 540	4350 ± 980	1950 ± 440
Maximum M_w^*	7.2 ± 0.1	6.8 ± 0.1	7.4 ± 0.1	7.6 ± 0.1	7.3 ± 0.1
Seismic moment** (10^{27} dyne cm)	0.7 ± 0.2	0.20 ± 0.06	1.5 ± 0.4	3.0 ± 1.0	1.0 ± 0.3
Average displacement** (m)	1.7 ± 0.1	1.2 ± 0.1	2.0 ± 0.2	2.5 ± 0.5	1.9 ± 0.1
Recurrence interval (yr)	2100 ± 1300	1500 ± 950	2500 ± 1600	3100 ± 2000	2400 ± 1500

surface displacements expected for a maximum earthquake reactivating Villicúm–Pedernal segments (Table 6). For the Las Tapias segment, where compound scarps have been observed, the estimated average displacement is roughly on the order of 1.2 m (Table 6). Taking into account their vertical heights, the scarps that bound the A2 and the A3 surfaces may have experienced between three and seven and between eight and ten seismic events, respectively. In the case of maximum earthquakes reactivating both Villicúm and Las Tapias segments, the estimated average surface displacement is roughly on the order of 2 m, and the number of seismic events necessary to produce the scarps bounding A2 and A3 terraces are ranging between 2 and 4 and between 5 and 7, respectively. The topographic profile no 3 revealed a 60 cm high counter-slope that has been interpreted as the trace of the most recent seismic event on the Las Tapias segment. This small scarp is located on the A1 surface, where surficial processes are ongoing and its height is consistent with the assumption that it is degraded.

5.3 Recurrence interval

To estimate average recurrence intervals (RI) following the direct method (e.g. Wallace 1970), we used the lower bound of the long-term shortening rate (S) based on the cumulative displacements of the dated terraces and the average displacement estimated using the empirical relationships of Wells & Coppersmith (1994) and the scaling laws from Hanks & Kanamori (1979):

$$RI = \frac{AD}{S}. \tag{9}$$

For the Las Tapias segment, a shortening rate of ∼0.8 (±0.5) mm yr^{-1} is estimated. Taking into account an average displacement of 1.2 (±0.1) m, estimated from Hanks & Kanamori (1979) (Table 6), a recurrence interval of 1.5 (±0.9) kyr may thus be calculated for the Las Tapias segment. This estimation is consistent with the observation of a 60 cm high, west-facing degraded slope younger than the age of the A1 surface (i.e. 1.5 (±0.8) ^{10}Be kyr). Assuming that the ∼1 mm yr^{-1} shortening rate calculated over ∼20 kyr is representative of the Quaternary shortening rate on the 65 km long Villicúm–Las Tapias segment, a recurrence interval of 2.4 (±1.5) kyr may be calculated using an average displacement of 1.9 (±0.1) m, which is probably underestimated (Table 6).

5.4 Did the Villicúm–Pedernal thrust break in 1944?

The destructive $M_s = 7.4$ San Juan earthquake occurred on 1944 January 15, producing a maximum intensity of IX in the city of San Juan (INPRES 1977). The location of this historical earthquake is poorly constrained: 31.6° ± 0.4°S and 68.5° ± 0.6°W (e.g. Kadinsky-Cade 1985), and International Seismological Centers reports a depth of 50 km. During this earthquake, only a few kilometre-long ruptures have been described. Among these surface ruptures, 30 cm of dip-slip movement that increased to 60 cm over a period of weeks, was observed on a 6 km long surface rupture at La Laja (Castellanos 1945; Groeber 1944). The La Laja fault is very unlikely to be the seismic source of this destructive event since moment magnitude (Hanks & Kanamori 1979; Kanamori 1983) and statistical relationships (Wells & Coppersmith 1994) indicate that a thrust-fault-generated earthquake with a magnitude of 7.2–7.4 should be characterized by a surface rupture length of the order of 50–60 km, which is close to the length of both Villicúm and Las Tapias segments. In the San Juan area, the seismic activity is concentrated beneath the Sierra Pie de Palo, the Tullúm Valley, the Eastern Precordillera, the Matagusanos valley and the easternmost Central Precordillera (Smalley *et al.* 1993). Nevertheless, even if earthquake hypocentres can define NW-dipping crustal scale fault planes locally, the dips, strikes and surface projections of the seismically defined structures do not correlate well with the faults and structures of the Eastern Precordillera (Smalley *et al.* 1993). An approach is to consider that the 1944 San Juan earthquake occurred on the Villicúm–Pedernal thrust, and more specifically on the 65 km long Villicúm–Las Tapias thrust that ramps below the Tullúm valley and Sierra Pie de Palo toward the east into a nearly 20–25 km deep

flat decollement suggested by the instrumental earthquake hypocentres (Smalley & Isacks 1990; Régnier *et al.* 1992; Smalley *et al.* 1993). Assuming that the most flat-lying part of the thrust should more probably behave aseismically, while the ramp part should have mainly stick-slip behaviour (e.g. Bombolakis 1992 and references herein), a ramp off the deep decollement then appears to be the most likely seismic source candidate for the 1944 San Juan earthquake (Fig. 1). Even if this destructive earthquake occurred at depth on the basal part of the thrust ramp, it did not produce large amounts of surface displacement, the induced deformation being most probably distributed through the Neogene foreland strata by flexural slip. The 60 cm high, west-facing upstream warp revealed by topographic profile no 3 corresponds to a slope that can be interpreted as the degraded trace of the most recent event on the fault that has ruptured the surface. Even if these anomalous drainage patterns cannot be dated more accurately than being younger than the A1 surface, that is 1.5 ($\pm$0.8) ^{10}Be kyr, one can make the hypothesis that they are associated with the 1944 San Juan earthquake. Nevertheless, this earthquake may have occurred on the ramp of Villicúm–Las Tapias thrust without producing any surface rupture, except for secondary fractures such as La Laja fault formed by coseismic and post-seismic flexural slip on bedding planes.

6 CONCLUSIONS

The Eastern Precordillera of San Juan is probably one of the most active zones of thrust tectonics in the world. Inversion of fault slip data provides new constraints on the stress regime associated with the growth of the Eastern Precordillera and shows that the development of the Eastern Precordillera is dominated by a pure compressive reverse faulting stress regime characterized by a N110 $\pm$ 10°E-trending compressional stress axis (σ_1). The data and observations reported in this current study lead us to consider the Villicúm–Pedernal thrust that borders the Eastern Precordillera between 31°S and 32°S latitude as the main ramp emergence of the basement decollement located at depth below the Tullúm Valley and Pie de Palo. This regional thrust is segmented into three thrust portions separated by fault branch zones where bedding-slip most probably results from flexural-slip faulting.

This study also provides new constraints on shortening rates occurring in the San Juan region. The geomorphic study realized along the 18 km long LTF combined with CRE ages shows that the minimum shortening rate calculated over the previous ~20 kyr is of the order of 0.8 mm yr^{-1}. This shortening rate is of the same order of magnitude as the ~0.9 mm yr^{-1} shortening rate determined further north by Zapata & Allmendinger (1996a) on Bermejo reverse structures. On a geological timescale, previous studies have shown that the deformation front of the Argentine precordillera have experienced a total shortening of ~40 km during the last 5 Myr, implying a mean geological slip rate of roughly 8 mm yr^{-1} (Jordan *et al.* 1993; Zapata & Allmendinger 1996a,b). This rate discrepancy may be reconciliated by arguing that this mean geological slip rate has to be taken into account by several individual thrusts that may act simultaneously or individually during the last 5 Myr, whereas the slip rate we determined on the Eastern Precordillera is associated with one single thrust. The earthquake moment tensor sum has been used to calculate a shortening rate caused by seismic deformation. This analysis of the focal solutions available for the last 23 yr shows that the seismic contribution may be three times greater than the shortening rate we determined for the Las Tapias fault over ~20 kyr using CRE dating. This same order of magnitude suggests strongly that the LTF is one of the major ramps of the Eastern Precordillera west-propagating thrust system. This interpretation is in agreement with a 0.9 mm yr^{-1} incision rate determined by U/Th dating of travertins located on the eastern flank of Villicúm range, in the La Laja area (Colombo *et al.* 2000), suggesting that the width of the uplifted zone is of the order of 7 km, in agreement with the proposed geometry for the Eastern Precordillera (Fig. 3).

From a seismic hazard point of view, the ramp that controls the development of the Eastern Precordillera appears to be one of the main potential seismic sources in the San Juan area, particularly the 65 km long Villicúm–Las Tapias segment. A first-order evaluation of the seismic hazard parameters shows that this 65 km long thrust segment can produce a maximum earthquake characterized by a magnitude of ~7.3 ($\pm$0.1) and a recurrence interval of 2.4 ($\pm$1.5) kyr. This part of the Villicúm–Pedernal ramp may have ruptured during the $M_s = 7.4$, 1944 San Juan earthquake producing very little surface rupture and only distributed flexural slip deformation on to the Neogene foreland bedding planes between the Eastern Precordillera and Pie de Palo.

ACKNOWLEDGMENTS

This study was realized within the co-operative agreement between ORSAYTERRE (UMR 8616, Université de Paris-Sud), the INPRES (Instituto Nacional de Prevención Sásmica) and the CEREGE (UMR CNRS 6635), Université d'Aix-Marseille III. We thank INPRES for fieldwork support. We thanks Gustavo Racciopi for helpful assistance in the field, J. Lestringuez and D. Deboffle at Centre de Spectrométrie Nucléaire et de Spectrométrie de Masse (IN_2P_3, Université Paris-Sud) for their continuing expertise in AMS measurements, and J.P. Villotte (ORSAYTERRE, UMR 8616, Université de Paris-Sud) for his technical help in sample preparation. The CNRS, CEA and IN_2P_3 support the Tandétron operation. Funding for the analyses was partly provided by the PROSE programme (INSU-CNRS). Special thanks are due to D. Schwartz, E.J. Brook and A. Meigs for remarks and criticisms that improved this paper considerably.

REFERENCES

Aki, K., 1966. Generation and propagation of G waves from the Niigata earthquake of June 16, 1964; Part 2, Estimation of earthquake moment, released energy and stress-strain drop from G wave spectrum, *Bull. Earthq. Res. Inst.,* **44,** 73–88.

Aki, K. & Richards, P.G., 1980. *Quantitative Seismology: Theory and Method,* W.H. Freeman, New York.

Angelier, J., 1990. Inversion of field data in fault tectonics to obtain the regional stress. Part II: a new rapid direct inversion method by analytical means, *Geophys. J. Int.* **103,** 363–376.

Baldis, B.A. & Chebli, G., 1969. Estructura profunda del área central de la Precordillera sanjuanina, *4° J. Geol. Argent.,* **1,** 47–66.

Baldis, B.A., Uliarte, E.R. & Vaca, A., 1979. Análisis estructural de la comarca sísmica de San Juan, *Asoc. Geol. Argent. Rev.,* **34,** 294–210.

Baldis, B.A., Beresi, M.S., Bordonaro, O. & Vaca, A., 1982. Síntesis evolutiva de la Precordillera de Argentina: Buenos Aires, Argentina, *5° Congreso Latinoamericano de Geología,* pp. 31–42.

Barazangi, M. & Isacks, B.L., 1976. Spatial distribution of earthquakes and subduction of the Nazca plate under South America, *Geology,* **4,** 686–692.

Bard, E. & Broecker, W.S., 1992. *The Last Deglaciation: Absolute and Radiocarbon Chronologies. Series I: Global Environmental Change,* Vol. 2, Springer-Verlag, Berlin.

Beer, J.A., Allmendinger, R.W., Figueroa, D.A. & Jordan, T.E., 1990. Seismic stratigraphy of a Neogene piggy-back basin, Argentina, *Am. Assoc. Petrol. Geol. Bull.,* **74,** 1183–1202.

Bellier, O. & Zoback, M.L., 1995. Recent state of stress change in the Walker Lane zone, western Basin and Range province. Unitated States, *Tectonics,* **14,** 564–593.

Bellier, O., Över, S., Poisson, A. & Andrieux, J., 1997. Recent temporal change in the stress state and modern stress field along the North Anatolian Fault Zone (Turkey), *Geophys. J. Int.* **131,** 61–86.

Ben-Menahem, A. & Singh, 1981. *Seismic Waves and Sources,* Springer-Verlag, New York.

Bierman, P.R., 1994. Using, *in situ*-produced cosmogenic isotopes to estimate rates of landscape evolution: a review from the geomorphic perspective, *J. geophys. Res.,* **99,** 13 885–13 896.

Bombolakis, E.G., 1992. A development stage of a foreland belt, in *Thrust tectonics,* pp. 33–40, ed. McClay, K.R., Chapmall & Hall, London.

Bordonaro, O., 1986. Bioestratigrafía del Cámbrico inferior de San Juan, IV, *Cong. Arg. Paleont. Biostrat.,* Mendoza, **1,** 19–27.

Bott, M.H.P., 1959. The mechanism of oblique slip faulting, *Geol. Mag.,* **96,** 109–117.

Brook, E.J. & Kurz, M.D., 1993. Surface exposure chronology using *in situ* cosmogenic ^{3}He in Antarctic quartz sandstone boulders, *Quatern. Res.,* **39,** 1–10.

Brown, E.T., Brook, E.J., Raisbeck, G.M., Yiou, F. & Kurz, M.D., 1992. Effective attenuation lenghts of cosmic rays producing ^{10}Be and ^{26}Al in quartz: implications for exposure age dating, *Geophys. Res. Lett.,* **19,** 369–372.

Brown, E.T., Bourlès, D.L., Colin, F., Raisbeck, G.M., Yiou, F. & Desgarceaux, S., 1995. Evidence for muon-induced production of ^{10}Be in near surface rocks from the Congo, *Geophys. Res. Lett.,* **22,** 703–706.

Brown, E.T., Bourlès, D.L., Burchfield, B.C., Qidong, D., Jun, L., Molnar, P., Raisbeck, G.M. & Yiou, F., 1998. Estimation of slip rates in the southern Tien Shan using cosmic ray exposure dates of abandoned alluvial fans, *Geol. Soc. Am. Bull.,* **110,** 377–386.

Brune, J.N., 1968. Seismic moment, seismicity and rate of slip along major fault zone, *J. geophys. Res.,* **73,** 777–784.

Cahill, T. & Isacks, B.L., 1992. Seismicity and shape of the Nazca Plate, *J. geophys. Res.,* **97,** 17 503–17 529.

Carey, E., 1979. Recherche des directions principales de contraintes associées au jeu d'une population de failles, *Rev. Géol. Dyn. Géogr. Phys.,* **21,** 57–66.

Carey, E. & Brunier, B., 1974. Analyse théorique et numérique d'un modèle mécanique élémentaire appliqué à l'étude d'une population de failles, *C.R. Acad. Sci. Paris,* **D279,** 891–894.

Carver, G.A. & McCalpin, J.P., 1996. Paleoseismology of compressional tectonic environments, in *Paleoseismology,* pp. 183–270, ed. McCalpin, J.P., Academic, San Diego, CA.

Castellanos, A., 1945. El terremoto de San Juan, in *Cuatro Lecciones Sobre Terremotos,* pp. 79–242, Asociación Cultural de Conferencias de Rosario, Argentina.

Cerling, T.E. & Craig, H., 1994. Geomorphology and *in situ* cosmogenic isotopes, *Ann. Rev. Earth planet. Sci.,* **22,** 273–317.

Chao Chung, L., & 67. coworkers, 1999. Surface ruptures along the Chelungpeu fault during the Chi-Chi earthquake, Taiwan, map published by Central Geological Survey, Ministry of Economic Affairs, Republic of China.

Chinn, D.S. & Isacks, B.L., 1983. Accurate source depths and focal mechanisms of shallow earthquakes in western South America and in the New Hebrides island arc, *Tectonics,* **2,** 529–563.

Clark, D.H., Bierman, P.R. & Larsen, P., 1995. Improving *in situ* cosmogenic chronometers, *Quatern. Res.,* **44,** 367–377.

Colombo, F., Busquets, P., Ramos, E., Vergès, J. & Ragona, D., 2000. Quaternary alluvial terraces in an active tectonic region: the San Juan River valley, Andean ranges, San Juan Province, Argentina, *J. South American Earth Sci.,* **13,** 611–626.

Cuerda, A.J., Cingolani, C.A., Varela, R. & Schawer, O.C., 1981. Geología de la Sierra de Mogna, Provincia de San Juan, *VII Congr. Geol. Arg.,* San Luis, **3,** 139–158.

Davies, G.F. & Brune, J.N., 1971. Regional and global fault rates from seismicity. *Nat. Phys. Sci.,* **229,** 101–107.

DePolo, C.M. & Slemmons, D.B., 1990. Estimation of earthquake size for seismic hazards, in *Neotectonics in Earthquake Evaluation,* pp. 1–28, eds Krinitsky, E.L. & Slemmons, D.B., *Geol. Soc. Am.,Rev. Eng. Geol.,* 8.

Dunai, T., 2000. Scaling factors for production rates of, *in situ* produced cosmogenic nuclides: A critical reevaluation, *Earth planet. Sci. Lett.,* **176,** 157–169.

Ego, F., Sebrier, M. & Yepes, H., 1995. Is the Cauca-Patia and Romeral Fault System left- or right-lateral?, *Geophys. Res. Lett.,* **22,** 33–36.

Engdahl, E.R., van der Hilst, R. & Buland, R., 1998. Global teleseismic earthquake relocation with improve travel times and procedures for depth determination, *Bull. seism. Soc. Am.,* **88,** 722–743.

Furque, G., 1983. Descripción geológica de la Hoja 19c, Ciénaga de Gualilán, Provincia de San Juan, *Serv. Geol. Nac. Bol.*

Gilbert, F., 1970. Excitation of the normal modes of the earth by earthquake sources, *Geophys. J. R. astr. Soc. London,* **22,** 223–226.

von Gosen, W., 1992. Structural evolution of the Argentine Precordillera: the Ró San Juan section, *J. Struct. Geol.,* **14,** 643–667.

Groeber, P., 1944. Movimientos tectónicos contemporáneos, Univ. Nac. La Plata, *Notas. Mus. Geol.,* **9,** 263–375.

Gutscher, M.A., Spakman, W. Bijwaard, H. & Engdahl, E.R., 2000. Geodynamics of flat subduction: seismicity and tomographic constraints from the Andean margin, *Tectonics,* **19,** 5, 814–833.

Hanks, T.C. & Kanamori, H., 1979. A moment magnitude scale, *J. geophys. Res.,* **84,** 2348–2350.

Instituto Nacional de Prevención Sísmica (INPRES), 1977. Zonificación Sísmica de la República Argentina, *Publ. Téc.,* **5,** San Juan, Argentina.

Instituto Nacional de Prevención Sísmica (INPRES), 1982. Microzonificación Sísmica del Valle de Tulum—Provincia de San Juan, *Informe Técnico General,* tres tomos, San Juan, Argentina.

Jackson, J. & McKenzie, D., 1988. The relationship between plate motions and seismic moment tensors, and the rates of active deformation in the Mediterranean and Middle East, *Geophys. J.,* **93,** 45–73.

Johnson, N.M., Jordan, T.E., Johnsson, P.A. & Naesser, C.W., 1986. Magnetic polarity stratigraphy, age and tectonic setting of fluvial sediments in an eastern Andean foreland basin, San Juan Province, Argentina, in *Foreland Basins,* pp. 63–75, eds Allen, P. & Homewood, P., *Int. Assoc. Sed. Spec. Pub.,* 8.

Jordan, T.E., 1995. Retro-arc foreland and related basins, in *Tectonics of sedimentary Basins,* pp. 331–362, eds Busby, C.J. & Ingersoll, R.V., Blackwell, London.

Jordan, T.E. & Allmendinger, R.W., 1986. The Sierras Pampeanas of Argentina: A modern analogue of Rocky Mountain foreland deformation, *Am. J. Sci.,* **286,** 737–764.

Jordan, T.E., Flemings, P.B. & Beer, J.A., 1988. Dating of thrust activity by use of foreland basin strata, in *New Perspectives in Basin Analysis,* eds Kleinspehn, K. & Paola, C., Springer-Verlag, New York.

Jordan, T.E., Isacks, B.L., Allmendinger, R.W., Brewer, J.A., Ramos, V.A. & Ando, C.J., 1983. Andean tectonics related to geometry of subducted Nazca plate, *Geol. Study Am. Bull.,* **94,** 341–361.

Jordan, T.E., Allmendinger, R.W., Damanti, J.F. & Drake, R., 1993. Chronology of motion in a complete thrust belt: the Precordillera, 30–31°S, Andes Mountains, *J. Geol.,* **101,** 135–156.

Jost, M.L. & Herrmann, R.B., 1989. A student's guide to and review of moment tensors, *Seism. Res. Lett.,* **60,** 2, 37–57.

Kadinsky-Cade, K., 1985. Seismotectonics of the Chile margin and the 1977 Caucete earthquake of western Argentina, *PhD thesis,* Cornell Univiversity, Ithaca, NY.

Kadinsky-Cade, K. & Reilinger, R., 1985. Surface deformation associated with the November 23, 1977, Caucete, Argentina, earthquake sequence, *J. geophys. Res.,* **90,** 12 691–12 700.

Kanamori, H., 1983. Magnitude scale and quantification of earthquakes, *Tectonophysics,* **93,** 185–199.

Kay, S.M., Maksaev, V., Moscoso, R., Mpodozis, C., Nasi, C. & Gordillo, C.E., 1988. Tertiary Andean magmatism in Chile and Argentina between 28°S and 33°S: correlation of magmatism chemistry with a changing Benioff zone, *J. South Am. Earth Sci.,* **1,** 21–38.

Kikuchi, M., Kanamori, H. & Satake, K., 1993. Source complexity of the 1988. Armenian earthquake: evidence of slow after-slip event, *J. geophys. Res.,* **98,** 15 797–15 808.

Kostrov, V.V., 1974. Seismic moment and energy of earthquakes, and seismic flow of rock, *Izv. Acad. Sci. URSS Phys. Solid Earth,* **1,** 23–44.

Lal, D., 1991. Cosmic ray labeling of erosion surfaces: *in situ* nuclide production rates and erosion models, *Earth planet. Sci. Lett.,* **104,** 424–439.

Lal, D. & Peters, B., 1987. Cosmic ray produced radioactivity on the Earth, in *Handbuch der Physik,* Vol. XLVI/2, pp. 551–612, ed. Flugg, S.

Langer, C.J. & Bollinger, G.A., 1988. Aftershocks of the Western Argentina (Caucete) earthquake of 23 November 1977: some tectonic implications, *Tectonophysics,* **148,** 131–146.

Luna, R.N., 1988. Evaluación estructural—Neotectónica de Lomas de Las Tapias, Provincia de San Juan, Trabajo final de Licenciatura, Universidad Nacional de San Juan, Argentina.

McDonough, M.R., Ramos, V.A., Isachsen, C.E., Bowring, S.A. & Vujovich, G.I., 1993. Edades preliminares de circones desl basamento de la Sierra Pie de Palo, Sierras Pampeanas Occidentales de San Juan: Implicancias para el supercontinente proterozoico de Rodinia, *XII Congr. Geol. Arg.,* **3,** 340–342.

Mercier, J.L., Carey-Gailhardis, E. & Sébrier, M., 1991. Paleostress determinations from fault kinematics: application to the neotectonics of the Hymalayan-Tibet and the Central Andes, *Phil. Trans. R. Soc. Lond.,* A., **337,** 41–52.

Milana, J.P., 1990. Sedimentologá y magnetoestratigrafía de formaciones Cenozoicas en el área de Mogna y su inserción en el marco tectonosedimentario de la Precordillera Oriental. *PhD thesis,* Universidad Nacional de San Juan, San Juan, Argentina.

Mirré, J.C., 1979. Descripción Geológica de la Hoja 19e, Valle Fértil, in *Secretaría de Minería de la Nación Argentina,* Boletín 147.

Molnar, P. & Ghose, S., 2000. Seismic Moments of Major Earthquakes and the Rate of Shortening across the Tien Shan, *Geophys. Res. Lett.,* **27,** 16, 2377–2381.

Nishiizumi, K., Kohl, C.P., Arnold, J.R., Dorn, I.R., Klein, J., Fink, D., Middleton, R. & Lal, D., 1993. Role of *in situ* cosmogenic ^{10}Be and ^{26}Al in the study of diverse geomorphic processes, *Earth Surface Processes,* **18,** 407–425.

Ortíz, A. & Zambrano, J.J., 1981. La provincia geológica Precordillera Oriental: San Luis, *VIII Congr. Geol. Arg.,* **3,** 59–74.

Raisbeck, G.M., Yiou, F., Bourlès, D.L., Lestringuez, J. & Deboffle, D., 1987. Measurements of ^{10}Be and ^{26}Al with a Tandetron AMS facility at Gif-sur-Yvette, *Nuc. Instr. Meth. Phys. Res.,* **B29,** 22–26.

Raisbeck, G.M., Yiou, F., Bourlès, D.L., Brown, E.T., Deboffle, D., Jouhanneau, P., Lestringuez, J. & Zhou, Z.Q., 1994. Measurements of ^{10}Be and ^{26}Al with a Tandetron AMS facility at Gif-sur-Yvette: progress, perturbations and projects, *Nuc. Instr. Meth. Phys. Res.,* **B92,** 43–46.

Régnier, M., Chatelain, J.-L., Smalley, R. Jr., Chiu, J.-M., Isacks, B.L. & Araujo, M., 1992. Seismotectonics of the Sierra Pie de Palo, a basement block uplift in the Andean foreland, *Bull. seism. Soc. Am.,* **82,** 2549–2571.

Ritz, J.F., Brown, E.T., Bourlès, D.L., Philip, H., Schlupp, A., Raisbeck, G.M., Yiou, F. & Enktuvshin, B., 1995. Slip rates along active faults estimated with cosmic-ray exposure dates: Application to the Bogd fault, Gobi-Altaï, Mongolia, *Geology,* **23,** 1019–1023.

Robinson, C., Raisbeck, G.M., Yiou, F., Lehman, B. & Laj, C., 1995. The relationship between ^{10}Be and geomagnetic field strength records in central North Atlantic sediments during the last 80 ka, *Earth planet. Sci. Lett.,* **136,** 551–557.

Sharma, I. & Middleton, R., 1989. Radiogenic production of ^{10}Be and ^{26}Al in uranium and thorium ores: Implications for studying terrestrial samples containing low levels of ^{10}Be and ^{26}Al, *Geochim. Cosmochim. Acta,* **53,** 709–716.

Siame, L.L., 1998. Cosmonucléide produit *in-situ* (^{10}Be) et quantification de la déformation active dans les Andes Centrales, *PhD thesis,* Université de Paris-Sud, Orsay, France, p. 373.

Siame, L.L. *et al.*, 1997a. Cosmogenic dating ranging from 20 to 700 ka of a series of alluvial fan surfaces affected by the El Tigre Fault, Argentina, *Geology,* **25,** 975–978.

Siame, L.L., Sébrier, M., Bellier, O., Bourlès, D.L., Castano, J.-C. & Araujo, M., 1997b. Geometry, segmentation and displacement rates of the El Tigre fault, San Juan Province (Argentina) from SPOT image analysis and ^{10}Be datings, *Annales Tectonicae,* 1–2, 3–26.

Smalley, R. Jr. & Isacks, B.L., 1990. Seismotectonics of thin and thick-skinned deformation in the Andean foreland from local network data: Evidence for a seismogenic lower crust, *J. geophys. Res.,* **95,** 12 487–12 498.

Smalley, Jr. R., Pujol, J., Régnier, M., Chiu, J.-M., Chatelain, J.-L., Isacks, B.L., Araujo, M. & Puebla, N., 1993. Basement seismicity beneath the Andean Precordillera thin-skinned thrust and fold belt and implications for crustal and lithospheric behaviour, *Tectonics,* **12,** 63–76.

Stone, J.O., 2000. Air pressure corrections for exposure dating, *J. geophys. Res.,* **105,** 23 753–23 759.

Súarez, G., Molnar, P. & Burchfield, B.C., 1983. Seismicity, fault plane solutions, depth of faulting and active tectonics of the Andes of Peru, Ecuador and Southern Colombia, *J. geophys. Res.*, **88,** 403–428.

Vujovich, G.I. & Ramos, V.A., 1994. La faja de Angaco y su relación con las Sierras Pampeanas Occidentales, Argentina, 7^{e} *Congresso Geológico Chileno,* **1,** 215–219.

Wallace, R.E., 1970. Earthquake recurrence intervals on the San Andreas Fault, *Geol. Soc. Am. Bull.,* **81,** 2875–2890.

Wells, D.L. & Coppersmith, K.J., 1994. New empirical relationships among magnitude, rupture lenght, rupture width, rupture area and surface displacement, *Bull. seism. Soc. Am.,* **84,** 974–1002.

Zapata, T.R., 1998. Crustal structure of the Andean thrust front at 30°S latitude from shallow and deep seismic reflection profiles, Argentina, *J. South Am. Earth Sci.,* **11,** 131–151.

Zapata, T.R. & Allmendinger, R.W., 1996. Thrust-front zone of the Precordillera, Argentina: a thick-skinned triangle zone, *Am. Assoc. Petrol. Geol. Bull.,* **80,** 359–381.

Zapata, T.R. & Allmendinger, R.W., 1996. Growth stratal records of intantaneous and progressive limb rotation in the Precordillera thrust belt and Bermejo basin, Argentina, *Tectonics,* **15,** 1065–1083.